frontiers | Frontiers in Earth Science

ORIGINAL RESEARCH
published: 17 August 2022
doi: 10.3389/feart.2022.886897

Petrogenesis of Havre Volcano in the Kermadec Arc: 2012 Eruption of a Chemically Homogeneous Rhyolite

J. Knafelc[1], D. Gust[1], S. E. Bryan[1], M. Anderson[2] and H. E. Cathey[1,3]*

[1]School of Earth and Atmospheric Sciences, Queensland University of Technology, Brisbane, QLD, Australia, [2]Department of Geological Sciences, University of Florida, Gainesville, FL, United States, [3]Central Analytical Research Facility, Queensland University of Technology, Brisbane, QLD, Australia

The 2012 Havre submarine eruption produced a 1.5 km^3 bulk rock volume or 0.52 km^3 dense rock equivalent volume of rhyolite emplaced as minor lava flows, a field of sunken seafloor pumice, and a volumetrically dominant pumice raft. This moderately large volume of medium-K (1.4–1.6 wt% K_2O) rhyolite pumice is relatively chemically homogeneous (71.5–73.0 wt% SiO_2), and no trace element variation or cryptic zoning has been detected despite the textural diversity of pumice material. Radiogenic isotope ratios ($^{87}Sr/^{86}Sr$ 0.703693–0.703744; $^{206}Pb/^{204}Pb$ 18.7648–18.7781; $^{208}Pb/^{204}Pb$ 38.587–38.605; $^{143}Nd/^{144}Nd$ 0.513001–0.513020) demonstrate the Havre rhyolite is sourced from mantle similar to regional eruptive products of the Kermadec arc volcanic front. Providing some further insight into the Havre magmatic system is an abundance of diverse volcanic rock fragments primarily embedded in the banded raft pumice. Embedded rock fragments represent a variety of fresh to hydrothermally altered lavas ranging in composition from basaltic to rhyolitic (50.6–72.3 wt% SiO_2) and are likely sourced from varying depths within the volcanic conduit during explosive fragmentation. The diverse embedded volcanic rock fragments, therefore, represent earlier erupted lavas that constructed Havre volcano and are snapshots of the petrogenetic history of Havre. Magnesian augite in basaltic to basaltic andesite embedded rock fragments has a similar compositional range ($En_{55}Fs_{12}Wo_{33}$ to $En_{39}Fs_{26}Wo_{35}$) to the previously documented antecrystic clinopyroxene observed in the 2012 rhyolite pumice raft. Herein, we explain how this large volume of chemically homogeneous crystal-poor rhyolite can be generated in an oceanic arc setting based on major and trace element petrogenetic models. Rhyolite-MELTS crystal fractionation models indicate the antecrystic mineral compositions within the Havre pumice of plagioclase ($An_{55–78}$), and magnesian augites ($En_{53}Fs_{10}Wo_{37}$ to $En_{40}Fs_{26}Wo_{34}$) are the primary phases that would crystallize in basaltic to andesitic melt compositions. Modeling indicates that the forerunner basaltic magma must be a relatively dry (~1 wt% H_20) low-K tholeiitic basalt in composition and would require ~78% crystallization at different pressures to ultimately generate the Havre 2012 rhyolite.

Keywords: Havre 2012 submarine eruption, crystal-poor rhyolite, crystal fractionation, rhyolite-MELTS, magmatic system, petrogenesis, Kermadec Arc

OPEN ACCESS

Edited by:
Arran Peter Murch, National Museum of Nature and Science, Japan

Reviewed by:
Simon James Barker, Victoria University of Wellington, New Zealand
Takashi Sano, National Museum of Nature and Science, Japan

****Correspondence:***
J. Knafelc
knafelc.joseph@gmail.com

Specialty section:
This article was submitted to Geochemistry, a section of the journal Frontiers in Earth Science

Received: *01 March 2022*
Accepted: *25 May 2022*
Published: *17 August 2022*

Citation:
Knafelc J, Gust D, Bryan SE, Anderson M and Cathey HE (2022) Petrogenesis of Havre Volcano in the Kermadec Arc: 2012 Eruption of a Chemically Homogeneous Rhyolite. Front. Earth Sci. 10:886897. doi: 10.3389/feart.2022.886897

INTRODUCTION

Submarine silicic volcanism along the Kermadec arc ridge has been associated with explosive eruptions, and some ancient explosive eruptions have produced calderas ranging from 1 to 7 km in diameter that reside in water depths of 200 to >2000 m (e.g., Macauley, West Rota, Healy, Havre: Barker et al., 2012; Rotella et al., 2015; Wright et al., 2006). The Havre 2012 rhyolite eruption is the largest recorded silicic submarine eruption by volume, evacuating an estimated 1.5 km^3 of rhyolite magma (Carey et al., 2014), and has recently been demonstrated to also have had an explosive phase (Knafelc et al., 2022). The 2012 Havre rhyolite eruption and the evidence for other rhyolite eruptions of significant volume in the Kermadec Arc place importance on understanding how relatively large volumes of silicic melts are generated and primed to erupt, potentially explosively in a deep-water volcanic arc setting (Rotella et al., 2015; Knafelc et al., 2022).

One of the challenges in understanding the petrogenesis of submarine island arc rhyolite magmas is the general lack of information on the longer-term magmatic systems of island arc volcanoes, where sampling may be restricted to small islands where the volcano has breached the surface (e.g., Raoul, Macauley; Smith et al., 2003a,b; Barker et al., 2012), where dredge surveys and sampling have been undertaken of the summit regions and flanks (Wright et al., 2006), or where products from recent eruptions have been sampled (Havre, Carey et al., 2018; Knafelc et al., 2020; 2022).

Petrogenetic models for rhyolite magma generation are recognized by two end-member mechanisms: *1*) extended fractionation of basaltic magma, that may occur over a range of pressures and may involve some crustal assimilation (Bachmann and Bergantz, 2004; Bachmann and Bergantz, 2008; Brophy, 2008; Cashman et al., 2017; Haase et al., 2011; Marxer et al., 2022) or *2*) partial melting of igneous arc crust (Deering et al., 2007; Smith and Price, 2006; Smith et al., 2003a; 2003b). Models for the petrogenesis of some Kermadec silicic magmas focus on either partial melting of arc igneous crust (Smith and Price, 2006; Smith et al., 2003a; 2003b) or extended fractionation of basaltic magma, possibly occurring over a range of pressures and with some crustal assimilation (Barker et al., 2013). Partial melting of amphibolite can generate dacite and rhyolite melts at relatively low degrees of melting (10%–15% melting; Brophy, 2008) with a characteristic LREE-depleted signature. With respect to the Havre silicic magmas, their lack of LREE-depleted signatures argues against a petrogenetic model involving amphibolite partial melting. Melting of the basaltic oceanic crust as an amphibole-free source may generate silicic melts. However, the need for large volumes of superheated basalt magmas to generate large volumes of melt from the dry mafic crust is unreasonable (Barker et al., 2013), and a deep crustal hot zone generated by basaltic underplating is more likely required (Annen et al., 2006). Given these limitations in determining what might be appropriate crustal materials and compositions to partially melt, we test the viability of a model that invokes extensive fractional crystallization. We have previously shown that the 2012 Havre medium-K rhyolite can be generated by limited fractional crystallization (7%) from a starting composition represented by a dredged Havre flank dacite (~67 wt% SiO_2; Knafelc et al., 2020). Herein, we explore the idea that this dacite composition is ultimately derived from a basaltic parent.

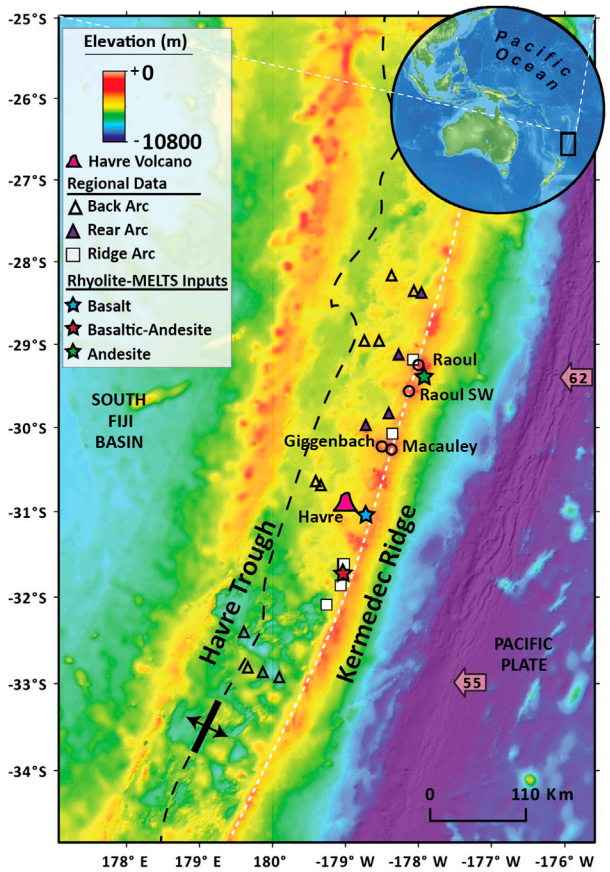

FIGURE 1 | Bathymetric map of the Kermadec subduction system. Havre volcano is denoted by a pink volcano symbol. Location of dredge samples from Hauff et al. (2021) is presented from the back-arc (open triangles), rear-arc (purple-filled triangles), and frontal ridge arc (white-filled boxes). Ridge-arc samples refer to samples dredged off the flank on the Kermadec Arc ridge inferred to be related to primary-arc magmatism. Rear arc samples refer to samples dredged off-axis to the west of primary volcanic arc ridge. Back-arc dredge samples refer to samples dredged from regions related to back-arc extension during the formation of the Havre Trough. Dredge compositions inputted in rhyolite-MELTS models are denoted by stars. The Kermadec frontal arc ridge, where most of the active arc volcanoes are located in the region, is denoted by the white dashed line. The Havre Trough back-arc basin spreading center is outlined by the back dashed line with arrows denoting the spreading direction. Bathymetric data are sourced from GEBCO-15 arc seconds of resolution (Tozer et al., 2019).

We present new major and trace element data on the full range of pumice types found in the Havre raft. Knafelc et al. (2020) first reported that a number of distinct pumice types occur in the raft deposits that differ in color, texture, and vesicularity. Further, the entire eruption had both explosive (Knafelc et al., 2022) and effusive phases (Carey et al., 2018; Ikegami et al., 2018; Manga et al., 2018). It, therefore, remains unclear if all the pumice

textural variation and different eruption styles have a compositional origin or record more syn-eruptive processes such as degassing and microlite crystallization promoting varied ascent rates and changed eruption styles. Herein, we test using rhyolite-MELTs and trace element crystal fractionation modeling the conditions that would be required to generate the Havre rhyolite by extended fractional crystallization from a basaltic parental composition. Radiogenic isotopic compositions ($^{87}Sr/^{86}Sr$; $^{206}Pb/^{204}Pb$; $^{208}Pb/^{204}Pb$; $^{143}Nd/^{144}Nd$) were also measured for raft and seafloor pumice and single lava flow to assess any isotopic heterogeneity between the erupted products and the regional eruptive products utilized here in fractionation models. This modeling can constrain the nature of the magmatic and plumbing system and whether multiple levels of magma accumulation and fractionation are required to ultimately produce an eruptive rhyolite magma.

Geologic Setting

The Kermadec Arc is principally controlled by subduction of the relatively old (>80 Ma) oceanic lithosphere of the Pacific plate converging to the NE beneath the Australian plate. The present-day magmatic expression includes both arc magmatism represented by submarine volcanoes located primarily along the Kermadec Ridge and crustal extension forming the Havre Trough back-arc region to the west (Smith and Price, 2006; **Figure 1**). The Havre Trough back-arc basin is in the early rifting stage of development. The present-day frontal arc (**Figure 1**) is mostly comprised of submarine volcanoes located along the Kermadec Ridge. The SE flank of Havre volcano merges into the Kermadec Arc ridge to the east (Wright et al., 2006), placing the volcano behind and off-axis to the west relative to the rest of the frontal volcanic arc. As most volcanoes in the Kermadec rear-arc are inactive, Havre and Giggenbach are both classified as active rear arc volcanoes (Gill et al., 2021).

Major and trace element data used in crystal fractionation models come from samples collected from the Havre Trough back-arc, Kermadec Arc Ridge, and Rear-Arc from 29 to 32°S (Hauff et al., 2021) and reconnaissance Havre dredge samples (Wright et al., 2006). Basaltic compositions in the region show a depletion of subduction slab influence from east to west and increasing water depth (Gill et al., 2021). Basaltic samples sourced from around the Havre volcano and from the frontal and rear arc generally have a tholeiitic low to medium-K composition (Gill et al., 2021). Havre volcano dredge samples that pre-date the 2012 eruption are primarily dacitic to rhyolitic lava flows, a few basalt-to-basaltic andesite lavas, and dacite to rhyolite pumice samples (Wright et al., 2006). These dredge samples are aphyric to moderately phyric (5%–20% crystals) with a phenocryst assemblage of plagioclase ± pyroxene and display a range of textures from non-vesicular, flow banded to pumiceous lavas (Wright et al., 2006).

The Havre 2012 Eruption

The Havre 2012 eruption is the largest silicic submarine eruption by volume recorded in historical times (Carey et al., 2014). The eruption produced a sizable bulk rock volume of 1.5 km^3 of rhyolite magma, where 80% (~1.2 km^3) of the erupted volume produced a pumice raft, and the remaining 20% (~0.3 km^3) formed lavas (0.21 km^3 dense rock volume; Carey et al., 2018) and deposits of pumice and >30 km^2 dm-thick ash layer (~0.7% bulk eruptive volume) on the volcano summit 900 m below sea level (Carey et al., 2018; Ikegami et al., 2018; Murch et al., 2019b; Mitchell et al., 2019; Murch et al., 2019a). The Havre raft and seafloor pumice have an averaged bulk density and dense rock equivalent density of 550 kg m^{-3} and 2350 kg m^{-3}, respectively (Carey et al., 2018). The dense rock equivalent (DRE) volume of all eruption products (i.e., the combined volume of the pumice raft, seafloor pumice, lava flows, and ash deposits) is 0.52 km^3 after removing the void space in the pumiceous eruptive products (raft and seafloor pumice).

The Havre 2012 eruption was initially recognized by a massive pumice raft on the ocean surface (Carey et al., 2014; Jutzeler et al., 2014). Pumice rafts are often associated with explosive submarine eruptions (Bryan et al., 2004; Bryan et al., 2012), and similarly, the Havre 2012 pumice was initially interpreted to have been produced by an explosive submarine eruption (Carey et al., 2014). An expedition to the Havre volcano in 2015 identified numerous new lava flows/domes, a field of giant seafloor pumice and ash at the volcanic summit of 900 mbsl (Carey et al., 2018, Ikegami et al., 2018, Murch et al., 2019a, b; Mitchell et al., 2019) that post-date previous observations of the Havre volcano (Wright et al., 2006). The lava flows and domes were clear indicators of an effusive phase for the Havre 2012 eruption. The similarity of appearance and chemical composition between the seafloor and raft pumice allowed for the assumption that these erupted products were produced contemporaneously, where their fate of floating to form the raft or sinking to the seafloor was attributed to the ability of a clast to retain enough isolated porosity to float (Manga et al., 2018). An effusive exit velocity of approximately 14 ms^{-1} was estimated to produce the pumice raft based on magma ascent models inputting seafloor pumice properties (Manga et al., 2018). However, more recent work has shown that when only utilizing seafloor pumice properties, eruption rates of the associated pumice rafts could be considerably underestimated (Knafelc et al., 2020; Mitchell et al., 2021; Knafelc et al., 2022). Most recently, the Havre 2012 eruption model has been expanded to include a short-lived, violent explosive eruption, capable of ejecting hot pyroclasts through the 900 m water column into the atmosphere, which then air-cooled to be deposited at the ocean surface, producing the pumice raft (Knafelc et al., 2022).

METHODS

This study utilizes regional geochemical and isotopic data (Wright et al., 2006; Hauff et al., 2021) from south of ~29–32°S in the Kermadec-subduction zone system to assess the petrogenesis of the Havre 2012 rhyolite (~31°S). Major and trace element data used in crystal fractionation models come from samples collected from the Havre Trough, Kermadec Arc Ridge, and Rear-Arc volcanoes from 29 to 32°S (Hauff et al.,

2021) and reconnaissance Havre dredge samples (Wright et al., 2006).

Sample Collection, XRF, and EPMA

Pumice collection, desalination of pumice samples prior to all chemical analysis, XRF whole-rock composition, and electron microprobe analysis (EMPA) of clinopyroxene within embedded rock fragments follow the methods presented in Knafelc et al. (2020). In order to desalinate the pumice samples prior to any bulk analysis (XRF & Solution ICP-MS), the pumice was crushed to roughly 1 mm in size fragments and placed in a forced convection hot bath (~50°C) of DI water for 2–3 weeks with the water replaced daily (further details described in Knafelc et al., 2020). Major and trace element data are presented for all types of pumice in the Havre 2012 pumice raft, a fraction of which were presented in Knafelc et al. (2020).

Five embedded rock fragments were analyzed for major (XRF) and trace elements (ICP-MS-Dissolution). Embedded rock fragments were analyzed if there was enough material for both XRF analysis (~0.1 g; LOI's not conducted due to limited material) and solution ICP-MS (~0.1 g) following thin section preparation. These samples were powdered using an agate mill, and only the interiors of the sample were crushed to assure no pumice glass contaminated the lithic fragment compositions. However, due to their small sizes, there is greater potential for these analyses to not truly represent the bulk composition of these rock fragments as skewed crystal to groundmass ratios could be distorting the overall composition.

ICP-MS-Dissolution Trace Element Acquisition

Trace element data were collected on 21 Havre 2012 raft pumice samples and the five embedded rock fragments contained in the Havre raft pumice.

Trace element data were obtained at the School of Earth and Atmospheric Sciences at QUT. Approximately 100 mg aliquots of powder from samples and geological reference materials were digested in screw-cap Savillex Teflon® beakers using HF-HNO_3 (3:1) on a hotplate at 150°C for 72 h. Sample conversion with HCl and HNO_3 followed before the residue was taken into a stock solution of ~20% HNO_3 with a gravimetric dilution factor of 1:100 (powder: solution). For analysis, a small (1.4 ml) aliquot was prepared gravimetrically with a dilution factor of 1:3800–5200 and 1:5000–6000 for Havre pumice samples and embedded rock fragments, respectively, in a 2% HNO_3 solution mixed element/enriched isotope internal standard (^{6}Li, ^{84}Sr, Rh, Re, Bi, ^{235}U) for analysis. Samples were injected by a syringe-driven autosampler (Cetac MVX-7100) into a tandem quadrupole-inductively coupled plasma-mass spectrometer (T-ICP-MS; Agilent 8900) at an uptake rate of ~100 µl/min.

Data were collected in no-gas mode and with oxide and dimer correction strategies adapted from Eggins et al. (1997), as explained in more detail in Ulrich et al. (2010). Final calibration of corrected signal intensities used the preferred composition of the USGS reference material USGS W-2a listed in **Supplementary Data S1** (see Kamber, 2009).

Reference materials were analyzed alongside unknowns for quality assurance. The mean concentrations of rock reference materials for the Havre pumice sample (USGS-W2 & JGS JB-2) and embedded rock fragments (USGS BIR-1 & JGS JB-2) from this study are reported alongside sample data in **Supplementary Data S1**. The internal precision for most trace analyses was <2%, and accuracy, estimated from repeat measurements of reference materials (relative to the values in Kamber, 2009) over the duration of the study, was better than 2% for most elements and better than 5% for less homogenously distributed metals (Kamber and Gladu, 2009).

LA-ICP-MS-Clinopyroxene

In situ trace element analysis of clinopyroxene in embedded rock fragments was carried out in July 2021 at the Central Analytical Research Facility at the Queensland University of Technology on the Agilent 7900 ICP-MS, coupled with Teledyne-Analyte Excite +, 193 nm Excimer ATL Laser Ablation system. Ablations were performed in He with a flow rate of 600 ml min^{-1}. Analysis used a laser fluence of 2.26 J cm^{-2}, an ablation time of 30 s, and a spot size of 40 µm. Trace element analysis was standardized to a primary and secondary glass standard of BCR2 and NIST612 and augite calcium concentrations previously obtained by electron microprobe (Ca wt% ~14.0 wt%) as an internal standard. Results are standardized utilizing the Iolite software (Woodhead et al., 2007; Paton et al., 2011). Accuracy and precision were monitored using secondary glass standards of NIST612 and BHVO-2G (http://georem.mpch-mainz.gwdg.de). Precision is better than 1%–6.5%, and accuracy is better than 6.5% for REE analysis (**Supplementary Data S1**). Accuracy for Ca is 11.2% and 4.7% on BHOV-2G and NIST612, respectively.

MC-ICP-MS-Radiogenic Isotopes

Radiogenic isotopes were analyzed for three raft pumice samples (two white and one banded), one seafloor pumice sample, and one groundmass glass from one of the seafloor lava flows (e.g., HVR-009; Ikegami et al., 2018) at the University of Florida, where approximately 50 mg of fresh, phenocryst-free glasses/pumices were handpicked using a binocular microscope. In order to remove seawater and sediment contamination, all samples were ultrasonically cleaned in DI water for 30 min and rinsed. Pumices were crushed and leached for 30 min in 2 N HCl, pipetted off and followed with DI rinsing. The rhyolite glass was leached and rinsed in 2 N HCl and then DI water. Sample dissolution procedures are described in detail in Anderson et al. (2021), and the Pb, Sr, and Nd chemical separation methods are detailed in Goss et al. (2010). Isotopic ratios were measured using a Nu-Plasma HR multicollector MC-ICP-MS using the methods described in Anderson et al. (2021) and Goss et al. (2010). To monitor instrument drift and ensure data quality, standards NBS-981, NBS-987, and JNDi-1 were run every five to six samples for Pb, Sr, and Nd, respectively. The reported $^{87}Sr/^{86}Sr$ ratios are relative to NBS 987 $^{87}Sr/^{86}Sr$ = 0.71024 (±0.00003, 2σ). The reported Nd isotopic compositions are relative to JNdi-1 $^{143}Nd/^{144}Nd$ = 0.512115 (±0.000017, 2σ), or ε_{Nd} = −10.2 (±0.3,

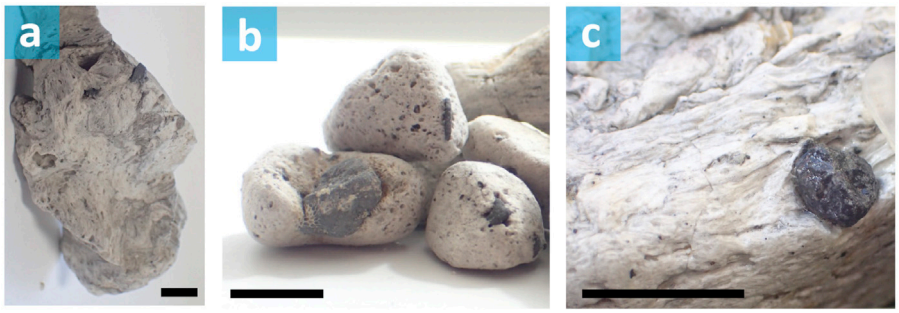

FIGURE 2 | Photographs of embedded rock fragments in the Havre 2012 pumice. **(A–C)** Representative photographs of embedded rock fragments within the 2012 pumice raft. Note that the black scale bar in each panel is equal to 1 cm.

2σ). The Pb isotope data are relative to the following NBS 981 values: $^{206}Pb/^{204}Pb$ = 16.937 (±0.004, 2σ), $^{207}Pb/^{204}Pb$ = 15.490 (±0.004, 2σ), $^{208}Pb/^{204}Pb$ = 36.695 (±0.009, 2σ).

RESULTS

Pumice Raft Characterization

The Havre 2012 pumice raft contains an apparent diversity of material based on the color and texture of pumice clasts (Knafelc et al., 2020, 2022; Mitchell et al., 2021). As first reported by Knafelc et al. (2020), five different pumice types have been identified in deposits from the pumice raft found across the SW Pacific (see **Supplementary figure S1** in Knafelc et al., 2020) and can initially be distinguished on color and texture, ordered here in relative abundance: *1*) white, *2*) banded white-grey, *3*) pink, *4*) grey, and *5*) brown**.** Despite the color and textural variation, the mineralogy remains consistent across the pumice types. The phenocryst/microphenocryst assemblage consists of plagioclase, orthopyroxene (enstatite), clinopyroxene (augite), and Fe-Ti oxides (titanomagnetite, ilmenite), with plagioclase being the dominant phenocryst phase (Knafelc et al., 2020). The characteristics of these pumice types are briefly summarized in **Supplementary Material S1**.

Embedded Rock Fragments

Embedded rock fragments are virtually unique to the raft banded pumice (see also Mitchell et al., 2021). Readily observable angular rock fragments are lapilli-sized (4–10 mm), but some are <2 mm in size (**Figure 2**). A single pumice clast can contain one or several rock fragments; at least five rock fragments have been observed in one pumice clast. Rock fragment size tends to correlate with pumice clast size, with the largest embedded rock fragments observed in the larger pumice clasts. Rock fragments are typically fine-grained and dark grey in color. More than 68 embedded rock fragments collected from multiple banded and white raft pumice clasts have been examined petrographically.

Embedded rock fragments are separated here into four groups based on texture, crystallinity, and mineral assemblages and are briefly summarized below. The phenocryst mineralogy is similar between the groups, but olivine and orthopyroxene have not been observed in any fragment. This has revealed that the embedded lithic clasts in the Havre raft pumice are lithologically diverse based on their distinct textures and mineral assemblages (**Figure 3**). All fragments are volcanic (i.e., lavas), and each lithic fragment group defined here contains samples with signs of varying degrees of hydrothermal alteration (i.e., devitrified glass and alteration minerals including clays and epidote). No plutonic or pyroclastic rock fragments have so far been observed.

Group 1 embedded rock fragments contain a phenocrystic assemblage of plagioclase ± clinopyroxene set in a hypocrystalline groundmass with varying proportions of clinopyroxene and plagioclase ± magnetite. Some rock fragments contain plagioclase phenocrysts with a groundmass dominated by clinopyroxene with minor proportions of plagioclase and magnetite (**Figures 3A,G**). In comparison, some rock fragments contain plagioclase and clinopyroxene phenocrysts set in a clinopyroxene-rich groundmass ± plagioclase (**Figures 3B,H**). The mineral assemblages suggest these rock fragments range in composition from basaltic andesite to andesite. Saussuritized plagioclase and clay alteration of clinopyroxene are common in the hydrothermally altered samples. Clinopyroxene is commonly subhederal to anhedral with clear resorbed rims, skeletal textures, and some hourglass zoning in both phenocryst and groundmass crystals.

Group 2 rock fragments have plagioclase microphenocrysts set in a hypocrystalline groundmass with a subtle alignment of plagioclase microlites producing a subtrachytic texture (**Figures 3C,I**). These lithic clasts present dark brown to black glass colors in plane light. Some Group 2 samples contain vesicles, or show evidence of plagioclase hydrothermally altering to clays. The plagioclase-rich characteristic of these rock fragments set in a dark-colored glass is characteristic of basaltic to basaltic-andesitic composition lava flows.

Group 3 comprises rock fragments that resemble the Havre 2012 rhyolite lava flows (Ikegami et al., 2018) with plagioclase and clinopyroxene phenocrysts set in a hypocrystalline glassy groundmass containing slightly oblate and elongated vesicles indicating flow (**Figures 3D,J**; vesicularity ~20%–30%). Embedded rock fragments of this type present variable alteration, most notable by varying degrees of devitrified glass and quartz-filled amygdules.

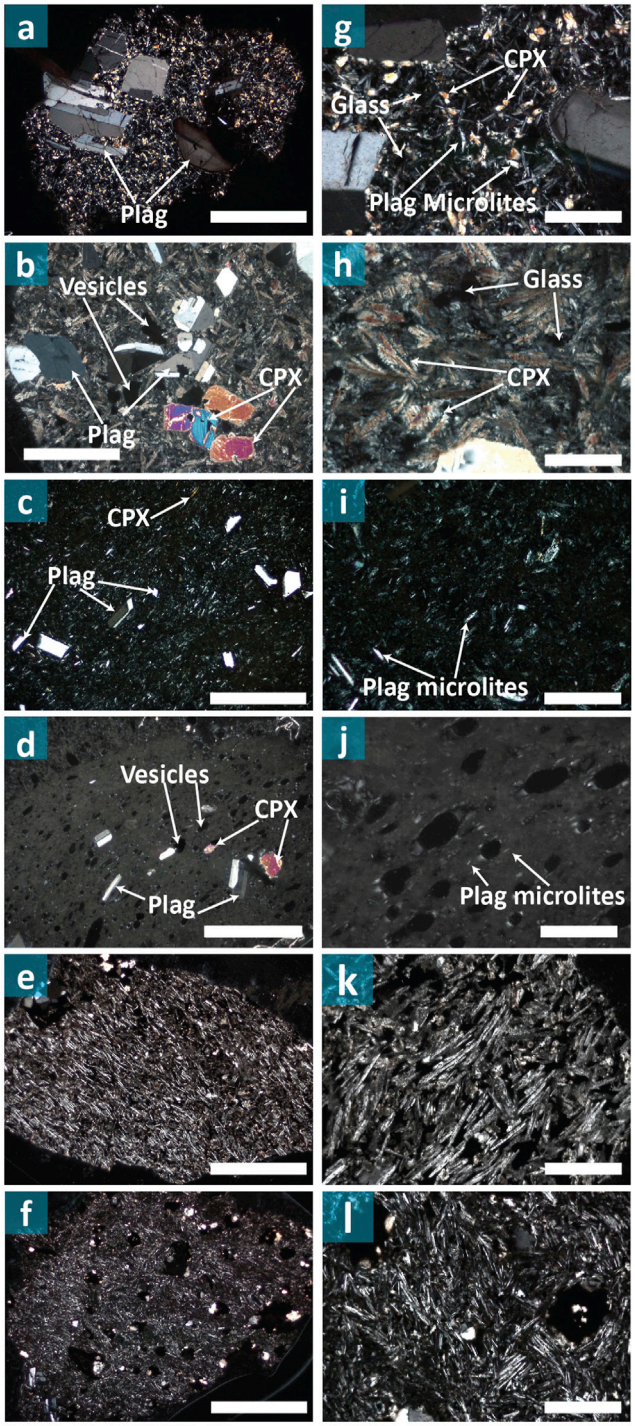

FIGURE 3 | Textural diversity of Embedded rock fragments within the Havre 2012 pumice raft. **(A–F)** Photomicrographs of rock fragments macro textures **(A,G)** denoting primary phenocryst phases and **(G–L)** groundmass textures correlating to the image in the left-hand column. **(A,G,B,H) Group 1** Rock fragments display porphyritic textures and hypocrystalline groundmasses of variable mineral assemblages. **(A,G)** Example of a group 1 rock fragments containing plagioclase phenocrysts set in a clinopyroxene-rich groundmass ± plagioclase and Fe-Ti oxides. **(B,H)** Example of a Group 1 rock fragment containing phenocrysts of plagioclase and clinopyroxene set in a

(*Continued*)

FIGURE 3 | groundmass that is plagioclase-rich ± clinopyroxene. **(C,I) Group 2** lithic example with plagioclase microproporphyritic texture in a hypocrystalline plagioclase groundmass. **(D,J) Group 3** rock fragments are vesiculated plagioclase-clinopyroxene phyric with a hypohyaline groundmass similar to Havre 2012 lava flows. **(E,K,F,L) Group 4** rock fragments resemble lava flows with varying degrees of trachytic plagioclase microlite textures ranging to hyalopilitic plagioclase +/- clinopyroxene (LF-1, LF-2). All panels are cross polarized light photomicrographs with scale bars equal to 1 mm. CPX and Plag refer to clinopyroxene and plagioclase, respectively.

Group 4 rock fragments are aphyric and contain plagioclase microlites with trachytic textures ranging to hyalopilitic plagioclase ± clinopyroxene (**Figures 3E,F,K,L**) characteristic of intermediate composition lavas. Some Group 4 rock fragments show weak signs of devitrification of a brown cloudy interstitial glass associated with sieve-textured plagioclase rims. Some samples also contain quartz-filled amygdules.

Geochemical Analyses

Data Integrity

Subtle Na concentration differences and Sr variability in otherwise isotopically homogenous pumice samples are likely due to the decrease in the effectiveness of the desalination method for microvesicular and/or pumiceous samples with greater apparent isolated porosity (i.e., banded, grey, and bread crusted raft pumice). This is evident for these microvesicular samples with much larger LOI (~2.1–3.6 wt%) compared to the more vesicular white and pink raft pumice (LOI = 1.3 wt%).

Embedded rock fragments were only analyzed if there was enough material for XRF and ICP-MS-dissolution after thin section preparation. Due to the small size of the lithic fragment samples (0.1 g per analysis type), their geochemical analysis appears to be distorted by large clusters of phenocrysts in some samples. This is evident as embedded rock fragments show relatively enriched Al, Ca, and Fe/Mg ratios and reduced Na contents (**Table 1**) compared to regional samples with similar silica contents (**Figures 4A–C**). These elements would notably be skewed by the presence of either plagioclase (Ca and Al), clinopyroxene (Ca, Mg, and Fe), or hydrothermal alteration (Na), which are all observed in these embedded rock fragments (**Figure 2** and **Supplementary Figure S1**). Therefore, the data presented here for embedded rock fragments are used for basic characterization and are not used in the stepwise crystal fractionation models. However, the lithic fragment data still provide some insight into the chemical evolution of the Havre volcanic plumbing system and their relation to the regional data set of Hauff et al. (2021) that is utilized here in crystal fractionation models.

Havre 2012 Whole-Pumice Major and Trace Element Composition

Major element compositions are reported in **Table 1**, which combines the major element data reported by Knafelc et al. (2020) with additional results of major element analyses of Havre raft pumice. In addition, trace element results are

TABLE 1 | Major (XRF; weight percent oxide normalized to anhydrous) and trace element (ICP-MS dissolution; ppm) compositions of the diversity of Havre 2012 Pumice raft types and embedded rock fragments.

Sample type	White pumice		Banded pumice		Grey pumice		Bread crusted		Embedded rock fragments				
wt.%	WP-1-FB	Ave. (*n* = 6)	BP-5-MB	Ave. (*n* = 5)	GP-2-BB	Ave. (*n* = 2)	BC-2-MB	Ave. (*n* = 6)	RF-1	RF-2	RF-3	RF-4	RF-5
SiO_2	72.35	72.49	72.37	72.42	73.03	73.03	72.54	72.63	58.73	59.72	52.20	50.57	72.32
TiO_2	0.47	0.46	0.47	0.47	0.48	0.48	0.44	0.45	1.13	1.06	0.60	1.11	0.45
Al_2O_3	14.02	13.95	13.87	13.76	13.75	13.75	13.86	13.79	15.47	15.40	18.17	19.10	14.19
FeO(T)	3.02	2.99	2.93	2.97	2.95	2.95	2.87	2.89	10.19	12.34	7.79	12.39	2.65
MnO	0.11	0.12	0.11	0.11	0.12	0.12	0.11	0.11	0.20	0.00	0.13	0.23	0.11
MgO	0.64	0.65	0.61	0.64	0.57	0.57	0.63	0.59	3.14	1.17	6.26	9.91	0.83
CaO	2.76	2.59	2.52	2.54	2.52	2.52	2.43	2.47	5.63	5.02	12.07	2.53	2.40
Na_2O	5.09	5.21	5.58	5.53	5.05	5.05	5.55	5.50	4.07	4.28	2.35	3.87	5.52
K_2O	1.45	1.46	1.46	1.47	1.46	1.46	1.49	1.49	1.14	0.83	0.35	0.17	1.46
P_2O_5	0.08	0.09	0.08	0.08	0.08	0.08	0.08	0.08	0.30	0.17	0.07	0.11	0.08
LOI	0.99	1.32	2.59	2.08	2.43	2.43	3.50	3.58	—	—	—	—	—
Total	99.4	100.2	100.4	99.8	98.5	99.1	100.1	99.6	99.9	99.8	99.8	99.9	99.4
Rb (ppm)	29.8	30.2	28.6	29.2	29.4	29.8	28.7	29.3	14.5	8.1	8.7	2.9	18.8
Sr	139	138	137	136	138	137	140	133	204	133	170	120	109
Y	42	43	41	41	43	43	42	42	29	18	14	13	31
Zr	185	188	180	182	190	189	183	186	76	48	42	49	135
Nb	2.3	2.4	2.5	2.3	2.7	2.5	2.3	2.3	1.4	0.8	2.0	0.8	1.8
Mo	1.5	1.6	1.4	1.5	1.5	1.5	1.5	1.6	1.1	1.7	1.3	1.2	1.1
Cs	1.4	1.4	1.3	1.3	1.4	1.4	1.4	1.4	0.1	0.2	0.4	0.1	0.2
Ba	447	452	430	441	443	448	454	455	342	204	117	39	367
La	12.5	12.7	12.8	12.5	12.3	12.6	12.6	12.7	6.4	4.3	3.6	3.1	9.8
Ce	31	32	32	31	31	31	32	32	16	11	9	8	25
Pr	4.7	4.7	4.7	4.6	4.6	4.6	4.6	4.6	2.6	1.7	1.4	1.2	3.6
Nd	21	22	21	21	21	21	21	21	13	8	7	6	16
Sm	5.7	5.8	5.6	5.6	5.6	5.7	5.7	5.7	3.9	2.5	2.0	1.8	4.3
Eu	1.5	1.5	1.4	1.5	1.5	1.5	1.5	1.5	1.3	1.1	0.7	0.8	1.2
Gd	6.4	6.5	6.2	6.3	6.4	6.4	6.4	6.4	4.8	3.0	2.4	2.2	4.8
Tb	1.1	1.1	1.1	1.1	1.1	1.1	1.1	1.1	0.8	0.5	0.4	0.4	0.8
Dy	7.2	7.2	6.9	7.0	7.2	7.2	7.1	7.1	5.2	3.3	2.6	2.4	5.3
Ho	1.6	1.6	1.5	1.6	1.6	1.6	1.6	1.6	1.1	0.7	0.6	0.5	1.2
Er	4.8	4.8	4.6	4.7	4.9	4.8	4.7	4.7	3.3	2.1	1.6	1.5	3.6
Tm	0.8	0.8	0.7	0.7	0.8	0.8	0.7	0.7	0.5	0.3	0.3	0.2	0.6
Yb	5.0	5.0	4.8	4.9	5.0	5.0	4.9	5.0	3.2	2.0	1.6	1.4	3.7
Lu	0.8	0.8	0.7	0.8	0.8	0.8	0.8	0.8	0.5	0.3	0.2	0.2	0.6
Hf	5.0	5.1	4.9	5.0	5.2	5.1	5.0	5.0	2.2	1.4	1.2	1.4	3.8
Tl	0.2	0.2	0.2	0.2	0.2	0.2	0.2	0.2	0.1	0.1	0.0	0.0	0.1
Pb	7.0	7.7	6.2	6.3	6.4	6.4	6.2	6.6	2.3	2.7	1.9	5.7	3.4
Th	2.7	2.8	3.1	2.8	2.7	2.7	2.6	2.6	1.1	0.7	0.7	0.7	2.1
U	0.9	0.9	0.9	0.9	1.0	1.0	0.9	0.9	0.4	0.3	0.2	0.2	0.7
P	385	387	369	370	366	361	376	365	1,255	602	330	561	268
Ti	2,722	2,741	2,524	2,666	2,771	2,734	2,627	2,658	5,847	3,955	3,257	5,389	1,866
Sn	4.2	6.1	1.7	2.2	1.8	1.8	1.8	2.2	1.2	0.9	1.2	1.1	1.4
Sb	0.1	0.1	0.1	0.1	0.1	0.1	0.1	0.1	0.1	0.1	0.1	0.1	0.1
Cd	0.1	0.1	0.1	0.1	0.1	0.1	0.2	0.1	0.1	0.0	0.1	0.1	0.0

One example of each Havre 2012 pumice type and the average composition of each type is represented here. Complete set of the major and trace element data is presented in ***Supplementary Excel File S1****. FeOT is recalculated from Fe2O3.*

reported for all samples (**Supplementary Data S1**). For the Havre 2012 eruption, 21 pumice raft samples have been analyzed, of which eight analyses are of white pumice (2 of which are pink), five banded pumice, two grey pumice, and six bread-crusted grey-to-brown pumice samples. Importantly, previous studies that reported compositions from the Havre 2012 eruption focused mainly on the seafloor deposits of giant pumice (Manga et al., 2018; Mitchell et al., 2019) and lava flows (Carey et al., 2018), whereas only white Havre pumice has been captured in full (major and trace elements) for the Havre pumice raft (Reagan et al., 2017).

Herein, we compare the Havre 2012 pumice raft whole-rock compositions (**Figure 4**) to the rock fragments embedded in banded raft pumice, seafloor pumice (Mitchell et al., 2019), lava flows/domes (Carey et al., 2018), and pre-eruption dredge samples (Wright et al., 2006). All Havre 2012 raft pumices analyzed here are medium-K rhyolites (**Figures 4A,B**; Knafelc et al., 2020) and have medium-FeO/MgO (FeO/MgO = 4.79 ± 0.28; **Figure 4C**). There

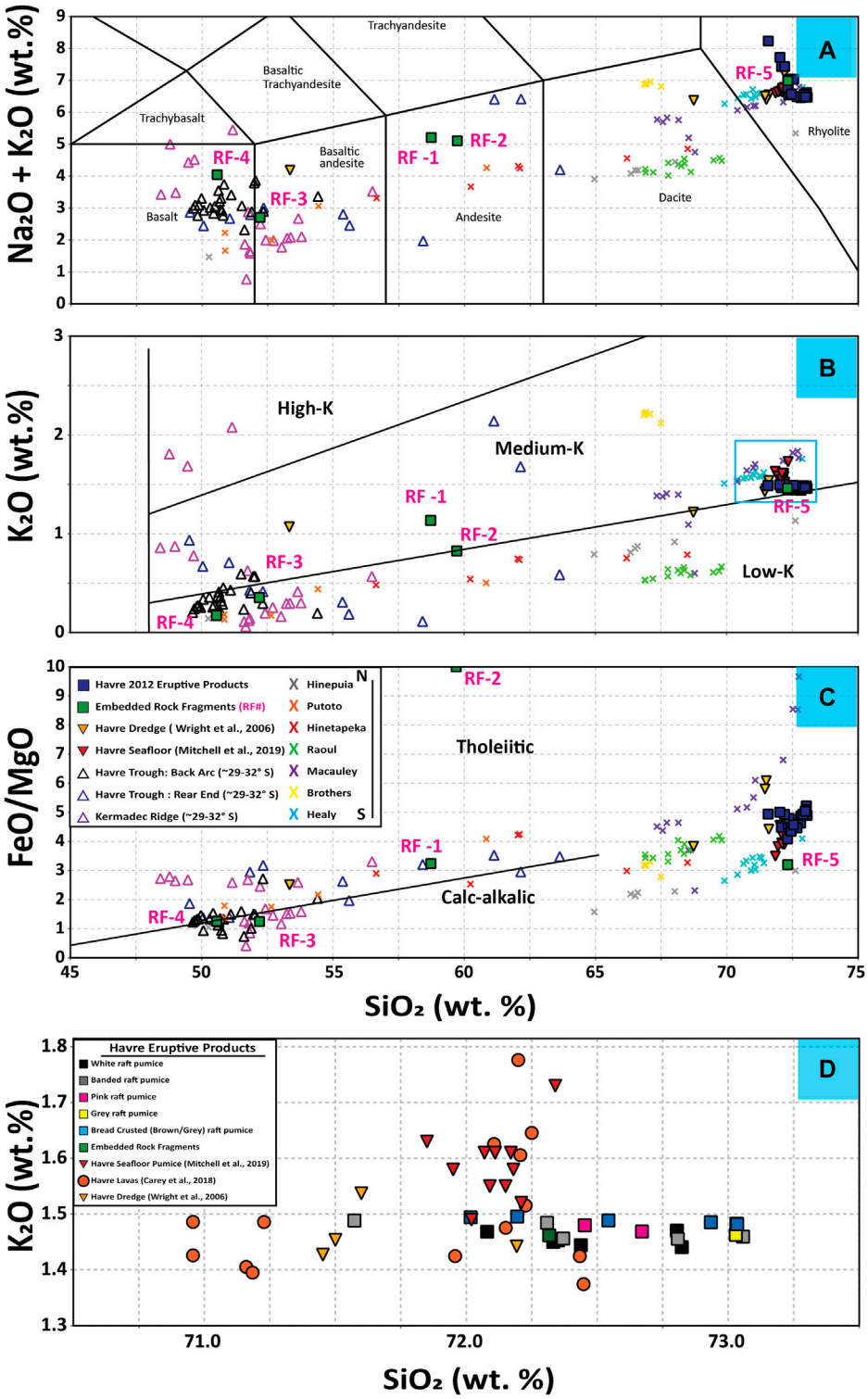

FIGURE 4 | Volcanic rock classification diagrams. **(A)** Total alkalis ($Na_2O + K_2O$ wt%) *versus* SiO_2 wt% (TAS) diagram from Le Maitre (1989). **(B)** SiO_2 *versus* K_2O with lines separating low-K, medium-K, and high-K boundaries (Gill, 1981). Note that the Havre 2012 eruptive products sit just above the low-K boundary near other rhyolites (e.g., Healy and Macauley) from the Kermadec Arc. The blue box outlines the area shown in panel **(D)**. **(C)** FeO/MgO *versus* SiO_2 where FeO is total Fe. The black line ($SiO_2 = 6.4*(FeO/MgO) + 42.8$) represents the boundary for calc-alkaline and tholeiitic melts following the classification scheme of Miyashiro (1974). Note that the Havre rhyolite products cannot be discriminated as either tholeiitic or calc-alkaline. Data presented here collected as a part of this study are shown as filled squares, with other data from the Havre eruption are plotted as filled upside-down triangles from the Havre 2012 seafloor pumice (red; Mitchell et al., 2019) and dredge samples that pre-dated the Havre 2012 eruption (gold; Wright et al., 2006). Additional dredge samples collected between ~29 and 32°S from the Havre Trough back-arc and rear end arc and Kermadec Ridge are shown here as open triangles sourced from Haueff et al. (2021); https://doi.org/10.26022/IEDA/111723). To compare other volcanic products produced in the Kermadec Arc, we present whole-rock chemistry from Hinepuia, Putoto, Hinetapeka, and Raoul from Timm et al. (2012) and Macauley, Brothers, and Healy volcanoes from Barker et al. (2013). **(D)** SiO_2 *versus* K_2O zoomed in on the rhyolite field of Havre eruptive products.

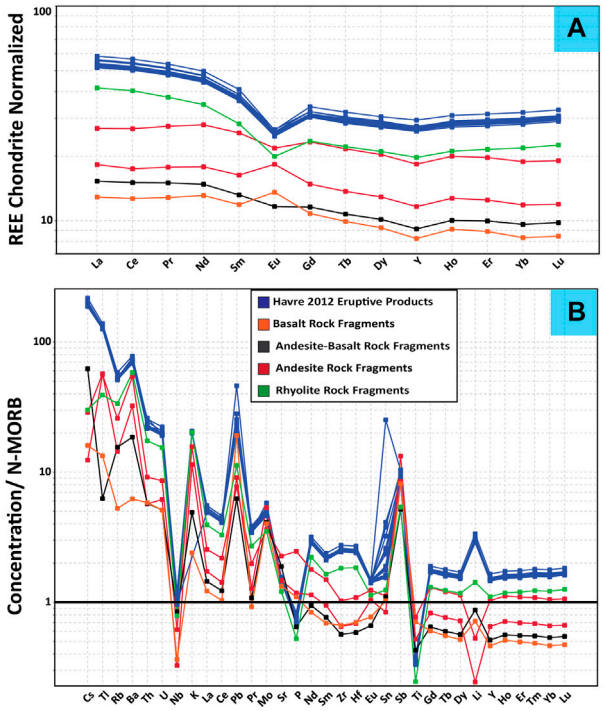

FIGURE 5 | Trace element spider diagrams of Havre 2012 pumice raft and embedded rock fragments. **(A)** Rare earth element spider diagram normalized to chondrite (McDonough at al., 1985). **(B)** Multi-element spider diagram normalized to N-MORB (Sun & McDonough, 1989).

are no apparent compositional differences between the visually diverse pumice types (**Figure 4D**). The Havre pumice raft, seafloor pumice, and lava flows group together at 72–73.5 wt% SiO_2, with only a small population of lava flows (Carey et al., 2018) that group at ~71–71.5 wt% SiO_2 (**Figure 4D**). Some seafloor and lava flows have subtly higher K contents than the raft pumice (**Figure 4D**). The 2012 Havre rhyolite is most closely related to the Healy rhyolite (Barker et al., 2012, 2013) in comparison to the other volcanic products presented here but is slightly more silicic and enriched in alkalis and Mg.

Both trace and major element compositions demonstrate that the Havre pumice is remarkably homogeneous with no systematic or cryptic changes among eruptive products (**Figure 5**). The homogeneity in major and trace elements in the Havre 2012 pumice implies that differences in the appearance of the pumice types are not related to magma composition. Except for Sr, the Havre 2012 rhyolite is enriched in fluid-mobile large ion lithophile elements (LILE: Cs, Rb, Ba, U, K). In comparison, the fluid-immobile, high field strength elements of Hf and Zr are only slightly enriched, whereas Ti and Nb are notably depleted (**Figure 5B**). The Havre pumice is LREE-enriched with La_{Ch}/Sm_{Ch} = 1.38 and has an Eu/Eu* = 0.74 ($Eu/Eu^* = Eu_{Ch}/(Sm_{Ch} \times Gd_{Ch})^{0.5}$; McLennan, 1989).

Embedded Rock Fragments

Major and trace element compositions are presented here for five embedded rock fragment samples. Due to the small mass of material available for analysis, sampling of larger crystals or alteration products could result in inaccurate whole-rock compositions of these embedded rock fragments. Therefore, we provide a more detailed petrographic description of these rock fragments in **Supplementary Figure S1**. Embedded rock fragments range in composition from basalt to rhyolite but with no analyzed dacite compositions (**Supplementary Figure S1F**). RF-1 and RF-2 are andesitic in composition consistent with the plagioclase-rich groundmass and the absence of larger phenocrysts similar to Group 4 embedded rock fragments (**Figures 3E,F,K,L**). However, RF-2 is altered with plagioclase altering to epidote group minerals and has an anomalously high FeO/MgO ratio compared to other samples with similar SiO_2 concentrations from the Havre Trough (**Table 1** and **Figure 4C**). RF-3 is basaltic andesite in composition with mineral assemblages and textures consistent with Group 1 embedded rock fragments (**Figures 3A,G**). RF-3 presents anomalously high Al_2O_3 and CaO contents compared to regional basaltic andesites, but in general clusters with other Kermadec arc ridge basaltic andesites in composition (**Figures 4A–C**). One rock fragment (RF-5) has a rhyolitic composition that closely resembles the Havre 2012 rhyolite (**Figures 4A–D**) composition; this rock fragment contains a similar micro-porphyritic groundmass to Group 2 embedded rock fragments, with phenocrysts of plagioclase and clinopyroxene.

Embedded rock fragments generally follow the same trend as the Havre pumice in LILE and HFSE element abundances on spider diagrams but are slightly more depleted overall. Lithic fragment REE patterns for a rhyolite lithic fragment are parallel to the Havre pumice but with more depleted concentrations. Variable Eu/Eu* ranging from 0.77 to 1.2 attests to differences in plagioclase abundance between the pumice and rock fragments (**Figure 5A**).

Augite Compositions in Embedded Rock Fragments

Single augite crystals in the Havre 2012 rhyolite pumice are interpreted to be antecrystic crystal cargo inherited from a crystal mush zone or earlier magma bodies based on augite crystallizing at temperatures much below pre-eruptive temperatures and these augites are in disequilibriumm with the host rhyolitic glass (Knafelc et al., 2020). Importantly, this could suggest that these antecrysts represent an earlier crystallization stage from a melt parental to the 2012 rhyolite. Similarly, augite is frequently observed in basaltic andesite Group 1 embedded rock fragments as phenocryst and groundmass phases. Here, we report the augite major and trace element compositions within Group 1 embedded rock fragments (**Supplementary Excel File S1**). Analysis of the augite compositions in the rock fragments provides a test for the provenance of the antecrystic augite in the 2012 pumice.

Clinopyroxene is observed in Group 1 embedded rock fragments as larger euhedral to subhedral phenocrysts with minor normal zoning (**Figures 6A,B**). Clinopyroxene also occurs as abundant subhedral groundmass microlites to microphenocrysts (**Figures 6C–E**) and displays a variety of

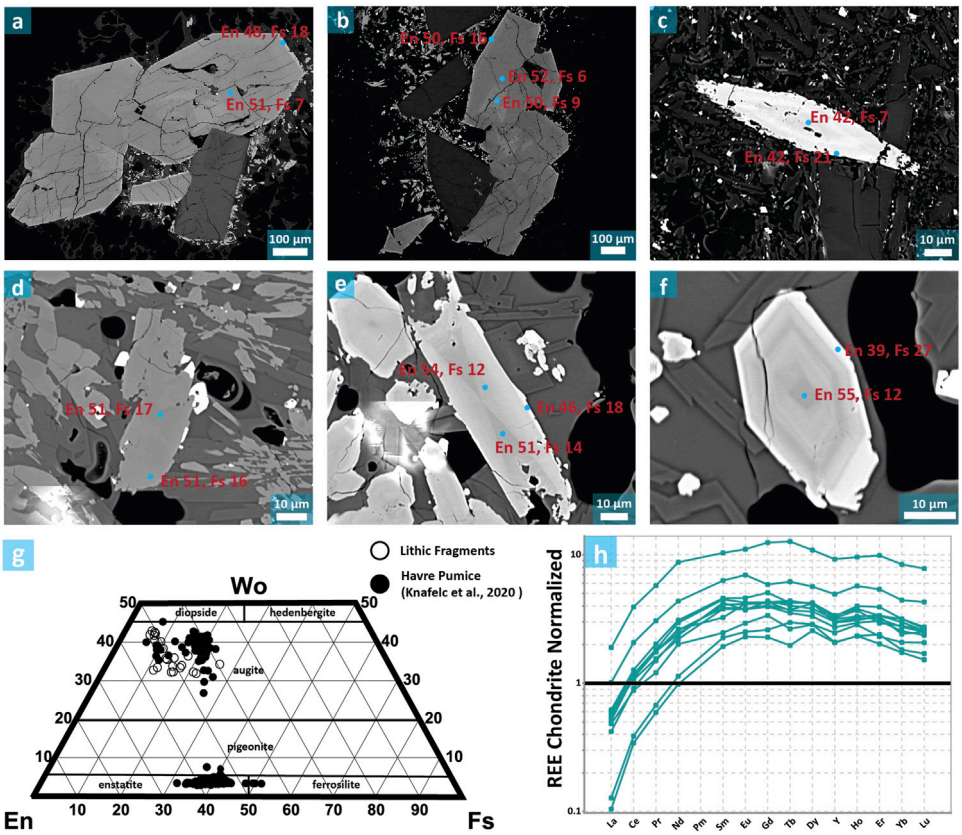

FIGURE 6 | Group 1 embedded rock fragments compared to Havre 2012 pumice. **(A–F)** Backscattered electron (BSE) images of clinopyroxene within Group 1 embedded rock fragments showing **(A,B)** larger phenocrysts with subtle normal zoning, **(C,D)** subhedral clinopyroxene microphenocryst with resorbed rims, **(E)** clinopyroxene with sector/hourglass zoning, and **(F)** clinopyroxene with oscillatory zoning. **(G)** Pyroxene quadrilateral diagram comparing the compositions of Havre rhyolite pumice antecrystic clinopyroxene from Knafelc et al. (2020) to clinopyroxene within Group 1 rock fragments (projection scheme of Lindsley and Andersen (1983). **(H)** REE contents of clinopyroxenes in rock fragments normalized to chondrite (McDonough et al., 1985).

textures, including resorption to skeletal textures (**Figures 6C,D**), sector zoning (**Figure 6E**), and complex oscillatory zoning (**Figure 6F**). End-member compositions (i.e., Wo, En, and Fs) have been calculated using the Lindsley and Anderson (1983) projection scheme that accounts for minor constituents. Clinopyroxenes have a range of compositions from $En_{55}Fs_{12}Wo_{33}$ to $En_{39}Fs_{26}Wo_{35}$ (**Figure 6G** and **Supplementary Excel File S1**). Group 1 augite compositions overlap the magnesian augite antecrystic population within the Havre 2012 rhyolite pumice raft (**Figure 6G**; Knafelc et al., 2020). In addition, the Havre magnesian augite is notably similar in composition to magnesian augite in the Sandy Bay Tephra rhyolite (Smith et al., 2003a) and augite included in pumice as antecrysts and within inclusions from Raoul, Macauley, and Healy (Barker et al., 2013). Rare earth element patterns for these augites are light rare-earth depleted relative to medium and heavy rare earth elements (**Figure 6H**). The trace element pattern is similar to that of the magnesian augite at Macauley and Healy (Barker et al., 2013), displaying increased Cr values with lower REE concentrations indicative of high-temperature crystallization during early crystallization or following a mafic recharge event.

Pb, Sr, and Nd Isotopes

Radiogenic isotopes which are unchanged during mantle melting and fractional crystallization are examined to assess the role of assimilation of any old and radiogenic crustal material that would have an isotopic distinction from a mantle source to generate this relatively large volume of rhyolite. First, the Pb, Sr, and Nd isotopic ratios of the Havre pumice (raft and seafloor) are remarkably similar to the Havre lava HVR-0009 (**Table 2**), regardless of their wide dispersal in the raft, consistent with these pumices and lava flows originating from the same magmatic system (**Figure 7**).

Second, the addition of a continental crust component would likely drive the $^{87}Sr/^{86}Sr$, $^{206}Pb/^{204}Pb$, and $^{208}Pb/^{204}Pb$ ratios up and the Nd isotopic ratios down (McCulloch et al., 1994; Plank and Langmuir, 1998). Only one pumice possesses slightly elevated $^{87}Sr/^{86}Sr$ (0.703962 ± 0.000011) relative to the other samples paired with identical Pb and Nd ratios, indicating that possible seawater contamination remained after cleaning the pumice (**Figure 7**). The rest of the samples are nearly indistinguishable with low Sr ratios ($^{87}Sr/^{86}Sr$ 0.703693–0.703744), low Pb ratios ($^{206}Pb/^{204}Pb$ 18.7648–18.7781 and $^{208}Pb/^{204}Pb$ 38.587–38.605), and elevated

TABLE 2 | Pb, Sr, and Nd isotope ratios of three raft and one seafloor pumice samples (*) and a single 2012 Havre lava glass (**), with the respective uncertainties (2 sd) reported.

Eruptive product	Lava	Raft pumice			Seafloor pumice
Sample	HVR_0009**	WP_B_MB*	WP_I_HI*	BP_5_MB*	GSFP_1*
$^{208}Pb/^{204}Pb$	38.605	38.589	38.601	38.590	38.587
2σ	0.002	0.002	0.003	0.002	0.003
$^{207}Pb/^{204}Pb$	15.6006	15.5982	15.5988	15.5971	15.5969
2σ	0.0007	0.0009	0.0010	0.0008	0.0010
$^{206}Pb/^{204}Pb$	18.7781	18.7655	18.7751	18.7690	18.7648
2σ	0.0009	0.0010	0.0011	0.0008	0.0013
$^{208}Pb/^{206}Pb$	2.05587	2.05636	2.05592	2.05597	2.05638
2σ	0.00003	0.00004	0.00004	0.00004	0.00004
$^{207}Pb/^{206}Pb$	0.830773	0.831208	0.830809	0.830974	0.831206
2σ	0.000010	0.000010	0.000014	0.000011	0.000013
$^{143}Nd/^{144}Nd$	0.513001	0.513020	0.513009	0.513002	0.513002
2σ	0.000005	0.000006	0.000005	0.000006	0.000004
$^{87}Sr/^{86}Sr$	0.703697	0.703693	0.703727	0.703744	0.703962
2σ	0.000011	0.000016	0.000015	0.000014	0.000011

Pb, Sr, and Nd isotope ratios were measured using a Nu-Plasma HR multicollector (MC) ICP-MS at the University of Florida using methods described in the text in Anderson et al. (2021) and Goss et al. (2010). Standards NBS-981, NBS-987, and JNdi-1 were run every five to six samples for Pb, Sr, and Nd, respectively.

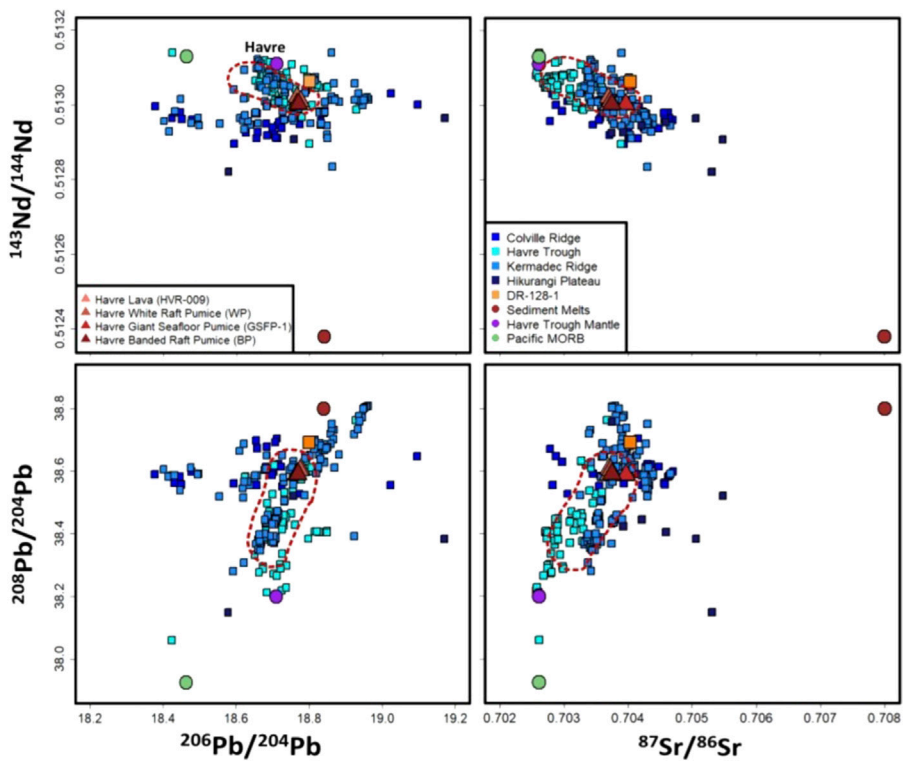

FIGURE 7 | Radiogenic isotope ratios (Pb, Sr, and Nd) of four Havre pumice and one Havre lava (triangles) compared with regional data (blue squares) for Kermadec Ridge, Havre Trough, Colville Ridge, and Hikurangi Plateau (Barker et al., 2013; Timm et al., 2014; Hauff et al., 2021). Havre lavas are outlined with a dashed red line. The orange square (DR-128–1) represents the isotopic composition of the parental basalt used for rhyolite-MELTS models. The pumice isotope ratios are identical to the Havre lava sample except for one pumice sample with a slightly elevated Sr ratio, consistent with seawater contamination. Local estimates of sediment melt (red circle), Havre Trough mantle (purple circle) from Haase et al. (2002), and average Pacific mid-ocean ridge basalts (green circle) from White et al. (1987) are also shown. The measured ratios from this study closely resemble mantle-derived basalts characteristic of the mantle in this region and do not suggest the assimilation of continental crust.

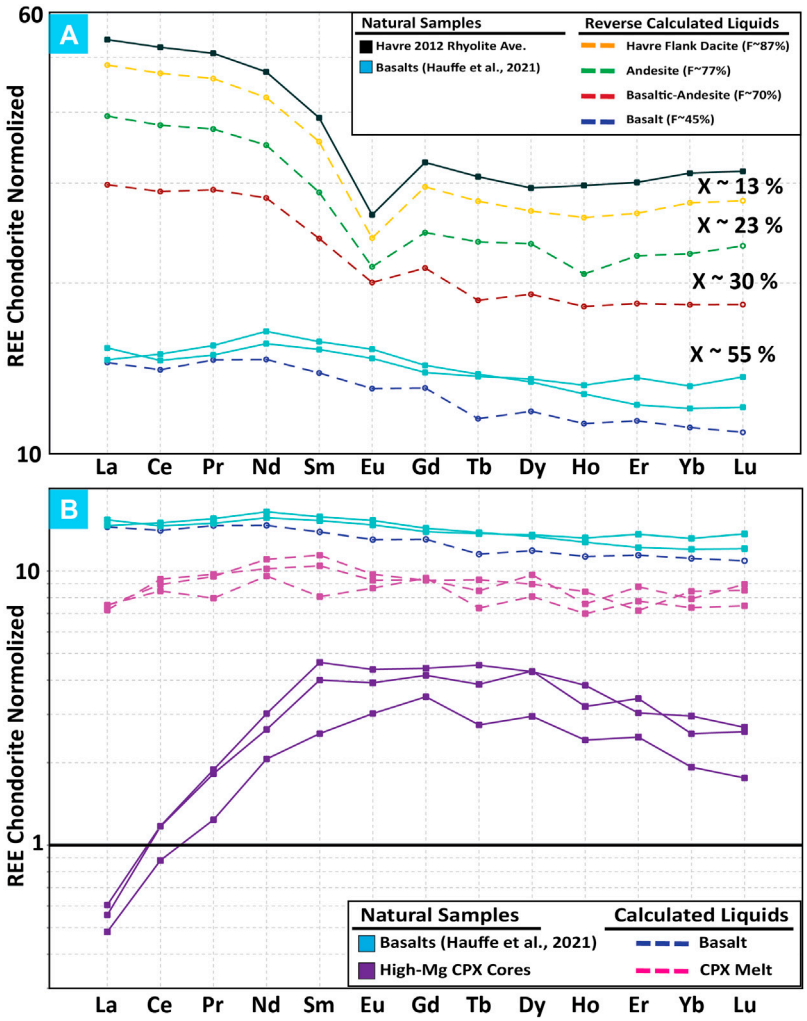

FIGURE 8 | Rare earth element (REE) reverse-calculated crystal fractionation models. **(A)** Reverse-calculated REE plots generated by reverse crystal fractionation modeling from an average Havre 2012 rhyolite trace element pattern (black solid line). Liquids for each calculated REE pattern (dashed lines) are generated by utilizing the mineral assemblage and proportions of each phase calculated in rhyolite-MELTS models incrementally from Havre 2012 rhyolite to Havre flank dacite to andesite to basaltic andesite to basalt compositions (**Table 3**). The percent of crystallization calculated in each step of the models is denoted by X%, and the REE patterns then correspond to the liquid (F) remaining for each rhyolite-MELTS modeling step. The resulting basalt calculated REE pattern is then compared to arc basalts from the regional data set (solid light blue lines; Hauff et al., 2021). **(B)** Calculated basaltic melt REE pattern (pink dashed lines) compared to the REE patterns of regional basalts and reverse-calculated basalt from the panel. The magnesium augite core REE patterns (solid purple lines) are utilized to calculate the REE patterns (dashed pink lines) of a basaltic melt; these magnesian augites would have crystallized from based on calculations from Sun and Liang (2012). All REE plots are normalized to chondrite (McDonough & Sun, 1985).

Nd ratios ($^{143}Nd/^{144}Nd$ 0.513001–0.513020) relative to continental crust and instead are isotopically similar to typical mantle-derived basalts regional to Havre volcano (**Figure 7**; McCulloch et al., 1994; Barker et al., 2013; Timm et al., 2014; Hauff et al., 2021; Gill et al., 2021). In addition, the 2012 Havre samples, such as other Kermadec arc eruptive products (Barker et al., 2013; Timm et al., 2104), display little signs of contamination from radiogenic crust or sediment-produced melts. Based on these observations, the following petrogenetic models evaluate the extent and conditions of crystal fractionation required to produce the homogeneous, mantle-like Havre radiogenic isotope ratios starting with a parental basalt sourced from the Kermadec Arc ridge with a similar mantle signature to dredge samples regional to Havre volcano (i.e., within 50–60 km or 0.5° latitude).

Rhyolite-MELTS Models

Here, we investigate the extent of crystal fractionation needed to produce the Havre 2012 rhyolite. The primary question is, what conditions are required for fractionation to successfully reproduce the medium-K Havre 2012 rhyolite? Fractionation would likely be stepwise and polybaric (*e.g.*, Marxer et al., 2022) and first require fractionation to produce an intermediate andesite composition from a parental arc basalt

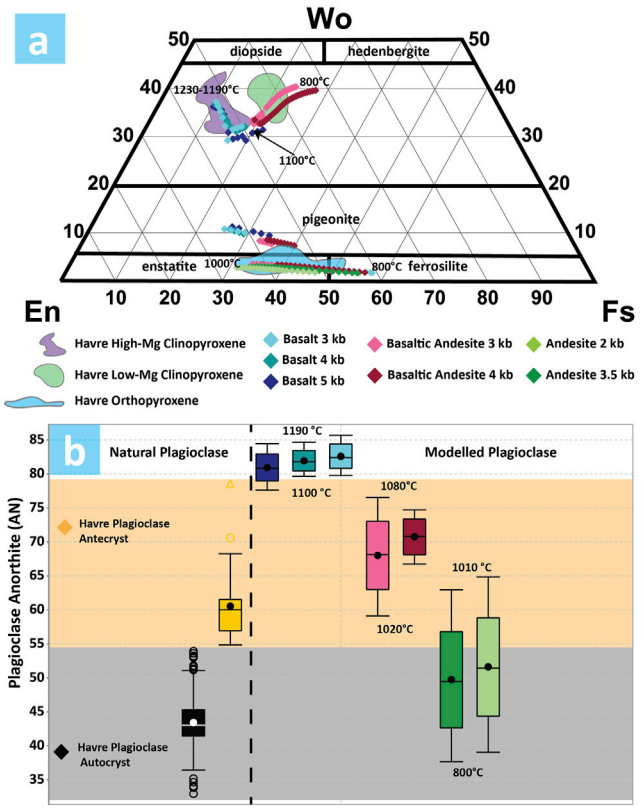

FIGURE 9 | Mineral chemistry comparison of measured Havre 2012 antecryst and rock fragment minerals *versus* rhyolite-MELTS calculated **(A)** clinopyroxene, orthopyroxene, and **(B)** plagioclase. **(A)** Rhyolite-MELTS model compositions are presented as closed diamonds with the color denoting the variable pressures of runs conducted for each step in crystal fractionation, where other initial conditions are presented in **Table 3**. Fields of color represent the measured populations of Havre clinopyroxene, with the purple field consisting of high-Mg clinopyroxene primarily observed in the Havre embedded rock fragments and Havre rhyolite, a green field of low-Mg clinopyroxene identified as antecrystic in the Havre 2012 rhyolite, and a blue field representing autocrystic orthopyroxene in the Havre 2012 rhyolite. **(B)** Box and whisker plots comparing the anorthite content of measured Havre (left of dashed black line) to the rhyolite-MELTS calculated plagioclase mineral chemistry (right of black dashed line). Havre 2012 plagioclase antecrystic cores ($An_{55–79}$) and autocrystic rims ($An_{34–55}$) are represented by the yellow and black fields, respectively. These natural ranges of plagioclase compositions are then compared to the calculated anorthite content from MELTS models. MELTS models are plotted in the same color as in panel **(A)** for the same model conditions. Note that high An content plagioclase is calculated primarily in basaltic to basaltic andesite models and autocrystic compositions are not produced until late in the andesite to dacite models.

that then fractionates to generate dacitic compositions, as reported at Havre (Wright et al., 2006). Previous modeling has indicated that only limited further fractionation (7%–14%) of the Havre dredge dacite composition (Wright et al., 2006) is required to produce the Havre 2012 rhyolite (Knafelc et al., 2020).

Rhyolite-MELTS models are used to test crystal fractionation as a mechanism for generating the rhyolite (**Figures 8–10**). One issue at Havre is relating the 2012 rhyolite to the small sample set of the Havre edifice to identify a potential basaltic parental composition. From Havre volcano, only a single basaltic sample was dredged prior to the 2012 eruption (i.e., 46–03; Wright et al., 2006). Rhyolite-MELTS models that utilize this Havre dredged basalt composition as a parental melt become too enriched in alkalis to replicate the 2012 rhyolite liquid composition even after only small degrees of crystallization (~7%). In the absence of a reliable basalt parental melt composition, specifically from the Havre volcano, a low-K tholeiitic basalt composition dredged in the region of Havre Volcano (**Figure 1**; DR-128-5; Hauff et al., 2021) is used as a parental composition. In addition, the parental basaltic composition used in rhyolite-MELTS models is isotopically similar (Gill et al., 2021) to the 2012 rhyolite and falls within the field of isotopic signatures from dredged samples from the region surrounding Havre volcano (i.e., within 50–60 km or 0.5° latitude from Havre). In combination, this provides confidence that this parental basalt had evolved from a similar source and was not strongly affected by any external contributions (**Figure 7**). Crystallization of this dry low-K-tholeiite basalt in rhyolite-MELTS models results in a liquid evolution that follows a medium pressure tholeiitic crystallization trend (Kuno, 1959) that leads to the flank dacite composition and then the erupted medium-K rhyolite composition on an AFM diagram (**Figure 10**). Collectively, these major and trace element models put possible constraints on the parental basalt composition, the conditions of potential storage zones through the crust (i.e., pressure/depth, temperature, and water content), and the sequence and extent of crystal fractionation required to generate the erupted rhyolite.

Modeling Conditions

The initial compositions and conditions of rhyolite-MELTS (Gualda et al., 2012; Ghiorso and Gualda, 2015) crystal fractionation models are presented in **Table 3**. We conducted rhyolite-MELTS models in three runs from the basaltic parent to basaltic andesite (DR126-1; Hauff et al., 2021) to andesite (DR-64-13: Hauff et al., 2021) to the flank dacite (HVR47-03; Wright et al., 2006). Knafelc et al. (2020) demonstrated a small degree of crystal fractionation ($F < 0.15$) of the Havre dacite melt composition (Wright et al., 2006) cooling from 950°C to a pre-eruptive temperature of 890 ± 27°C at 2–3 kbar and initial 4 wt% H_2O can generate the rhyolite liquid and autocrystic mineral assemblage. A water-saturated melt is produced allowing for vesiculation and explosive eruption to produce the large volume pumice raft. The models presented here were constrained to pre-eruptive conditions of the eruption based on autocrystic mineral chemistry barometers and geothermometers (Knafelc et al., 2020). Initial models are constrained to upper limits of the pressure of 5 kbar based on geophysical seismic models from multiple transects across the Kermadec arc ridge and back-arc, placing the crust-mantle boundary at Havre volcano at 12–15 km (Bassett et al., 2016). Therefore, crystal fractionation models are required to reach the parental dacite composition from more parental mafic melts at pressures of approximately 3–5 kbar, with residual water contents not greater than 4.0 wt%, and temperatures not higher than 950°–930°C. The calculated water content of the resulting liquid following each step of modeling is utilized as the initial water concentration for the subsequent initial water concentrations

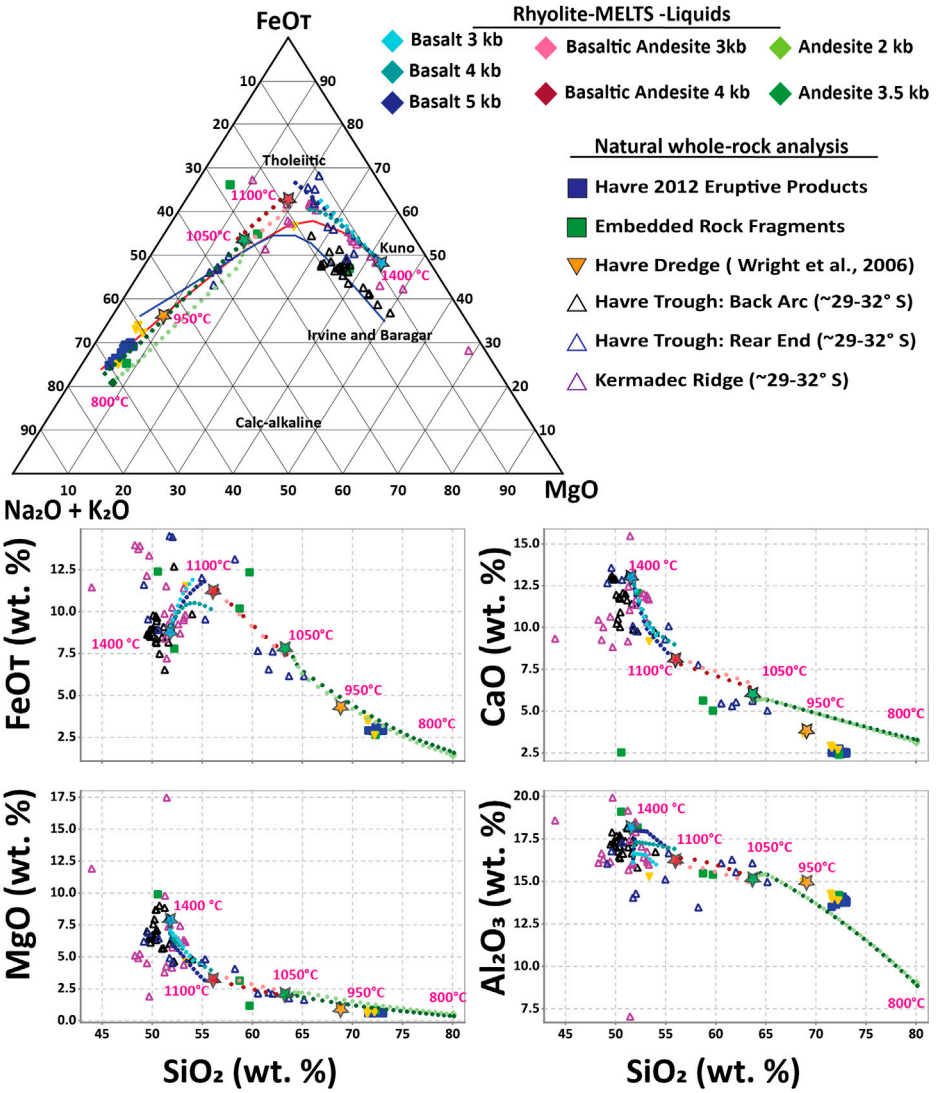

FIGURE 10 | Rhyolite-MELTS calculated liquids *versus* natural Kermadec arc compositions. Rhyolite-MELTS models calculated liquid lines of descent compared to measured whole-rock compositions of the Havre 2012 pumice and regional data sets. Rhyolite-MELTS models are presented as closed diamonds with the color denoting the variable pressures of runs conducted for each step in crystal fractionation, where other initial conditions are presented in **Table 3**. Initial compositions of each step of crystallization are presented by stars (i.e., basalt = blue, basaltic andesite = red, andesite = green, and the resulting Havre Flank Dacite = yellow) with pink text denoting the initial temperature of each model. Additional dredge samples collected between ~29 and 32°S latitude from the Havre Trough back-arc and rear-end-arc and Kermadec Ridge Arc are presented here as open triangles derived from Hauff et al. (2021):https://doi.org/10.26022/IEDA/111723.

in the models. To further verify the accuracy of our models, we compare rhyolite-MELTS calculated liquid compositions with the raft pumice and regional data set (Hauff et al., 2021). We also compare rhyolite-MELTS calculated mineral compositions to natural compositions and antecrystic populations of clinopyroxene and plagioclase (An >55) and autocrystic populations of orthopyroxene (Knafelc et al., 2020).

Crystallization Sequence

Rhyolite-MELTS calculated crystallization sequence incorporates multiple steps of crystal fractionation at progressively decreasing pressures (5–3 kb), increasing water concentrations (1–4 wt%), and increased oxygen fugacities (QFM to NNO +0.4) from a parental basalt sampled in the Havre volcano region (**Figures 1**, **7**) that ultimately can produce a compositionally similar liquid to the flank dacite (Wright et al., 2006). In basaltic models ranging from ~1200 to 1100°C, magnesian augite (initial composition ~ $En_{53}Fs_{10}Wo_{37}$) and pigeonite are the first crystallizing phases, followed by plagioclase ($An_{\sim 87}$). Approximately 55%–58% crystallization, dependent on pressure (5–3 kb), is required to generate a regional basaltic andesite composition melt and a gabbroic crystal cumulate at depth. In basaltic andesite models, continued crystallization of augite, pigeonite, and plagioclase with

TABLE 3 | Initial compositions and conditions of Rhyolite-MELTS models and resulting proportion of mineral phases fractionated normalized to 100 for use in trace element models. CPX, OPX, and plag are abbreviated for clinopyroxene, orthopyroxene and plagioclase, respectively.

Initial composition	Arc Basalt _DR-128-5 (1)	Basaltic Andesite_DR126-1 (1)	Andesite DR-64-13 (1)	Havre flank Dacite_47-03 (2)
SiO_2 wt%	51.8	56.1	63.1	68.7
TiO_2 wt%	0.60	0.94	0.83	0.68
Al_2O_3 wt%	16.14	16.22	15.05	14.99
FeO (T) wt%	8.98	11.23	7.78	4.15
MnO wt%	0.17	0.23	0.16	0.16
MgO wt%	7.54	3.40	2.23	1.08
CaO wt%	13.24	8.23	6.56	3.65
Na_2O wt%	1.52	2.94	3.58	5.16
K_2O wt%	0.12	0.56	0.58	1.22
P_2O_5 wt%	0.03	0.09	0.14	0.18
Water content (wt%)	1.00	2.50	3.50	4.00
Initial temperature °C	1400	1100	1050	950
Final temperature °C	1100	1020	950	890
Pressure (Kbars)	5 to 3	4 to 3	3.5 to 2	3 to 2
Oxygen fugacity	QFM	NNO	NNO	NNO +0.4
Fractionation (F)	55.2–58.9	29.6–33.7	22.6–12.9	12.7–7.00
Normalized combined (F)	55	13	7	3
CPX (augite + pigeonite)	66.5	39.8	0.0	0.0
Plag	33.5	44.0	60.1	79.6
Opx	0.0	0.0	23.1	2.7
Magnetite	0.0	16.2	16.8	15.7
Ilmenite	0.0	0.0	0.0	2.0
Total (normalized to 100)	100.0	100.0	100.0	100.0

Compositions noted (1) were sourced from Hauff et al. (2021) and modeled to generate the (2) Havre Flank dacite (Wright et al., 2006). The results of rhyolite-MELTS models from the Havre flank dacite are presented in Knafelc et al. (2020).

the addition of magnetite late in the sequence results in andesite liquid compositions such as those found in the regional data set after approximately 30%–34% crystallization dependent on pressure (4–3 kb) from 1100°C to 1020°C. In these basaltic andesite models, a shift in augite composition occurs where Mg content significantly reduces with decreasing temperature (**Figure 9**). Augite is no longer crystallized from andesitic melts. In andesite models, 23% to 13% crystallization of plagioclase, orthopyroxene, and magnetite over a temperature range of 1,020°C to 950°C is required to generate the Havre flank dacite liquid composition in 3.5 and 2 kbar pressure models, respectively.

Trace Element Models

Mineral assemblages and their respective proportions determined by rhyolite-MELTS (**Table 3**) are used to incrementally reverse-calculate a possible rare earth element (REE) pattern for a parental basalt from the Havre 2012 rhyolite through pure Rayleigh crystal fractionation (**Figure 8A**). Trace element composition of Havre 2012 rhyolite attests to the homogeneity of the erupted pumice raft (**Figure 6**), and, therefore, the average white raft pumice REE pattern is the initial composition used for reverse liquid quantifications. In the models, the degree of crystallization required to back-calculate from rhyolite to basalt, as well as in these early steps of crystallization (i.e., the steps from rhyolite to basaltic andesite), decreases. The resulting REE patterns remain parallel to the Havre 2012 rhyolite, whereas each element becomes more depleted while reducing the Eu anomaly in each step. The largest jump in crystallization from basaltic andesite to basalt (approximately 55% crystallization) flattens the REE pattern and eliminates the Eu anomaly, resulting in a similar pattern to some regional arc basalts (Hauff et al., 2021).

This reverse-calculated basalt REE pattern is then compared to calculated basaltic melt REE patterns (Sun and Liang, 2012) that could have crystallized the magnesian augite documented in rock fragment Group 1 (**Figure 8B**). The resulting REE patterns are determined from partition coefficients (Kds) calculated from magnesian augite cores' major element composition (Sun & Liang, 2012), assuming a temperature of 1230°C and 1 wt% H_20 (i.e., conditions an $En_{53}Fs_{10}Wo_{37}$ clinopyroxene first crystallizes in rhyolite-MELTS basaltic models). The calculated REE pattern for the augite calculated basaltic melts compare well with the regional basalts and are slightly more enriched than the reverse-calculated basalts. This result provides some confidence: *1*) magnesian augites found in embedded rock fragments were initially crystallizing from a parental mafic melt and *2*) assuming a fractionation origin, the parental basalt of the Havre 2012 rhyolite is likely similar in composition to the regional basalts with similarly flat REE patterns.

DISCUSSION

Chemical Homogeneity of the 2012 Havre Rhyolite Magma

A relatively chemically homogenous rhyolite magma body erupted during most of the Havre 2012 eruption (i.e., seafloor and pumice raft-producing phase of eruption). Only subtle chemical differences in major elements are resolvable between

raft pumice, seafloor pumice, and late-stage lava flows (**Figure 4** and **Table 1**). However, a cluster of lavas contains subtly lower silica contents relative to the pumice deposits and other lavas (Carey et al., 2018; **Figure 4D**). This population includes lava flows A-E that represent 0.05 km^3 (i.e., 10% of the total dense rock volume erupted) of rhyolite interpreted to have erupted months before the raft and seafloor pumice (Carey et al., 2018; Ikegami et al., 2018). Assuming the raft and seafloor pumice have erupted contemporaneously, the transition to an explosive eruption to produce the raft and seafloor pumice is unrelated to changes in bulk composition. This is evident through the whole-rock (major and trace element) homogeneity of the pumice deposits (**Figures 4D**, **5A**). Furthermore, the explosive eruption is triggered by spontaneous nanolite nucleation, resulting in increased viscosity, and enhanced volatile exsolution for material erupted to make the pumice raft (Knafelc et al., 2022), whereas seafloor pumice represents material absent of nanolites, and likely water quenched on the margins of the explosive eruption column. The change in eruption style from pumice raft production during an explosive phase to effusive producing later stage lava flows/domes (lava flows F-P) with a similar composition to the Havre pumice, most likely during the terminal phases of the eruption (Carey et al., 2018; Ikegami et al., 2018) is therefore not related to a change in magma composition (**Figure 4D**). A possible explanation for the subtle increase in silica content in the raft, seafloor, and lava flows/domes F-P is that these melts continued to crystallize, following emplacement of the earlier lower silica lava flows but prior to the main phase of explosivity.

The textural diversity of pumice types observed in the raft also does not record primary compositional variation. The visual and textural characteristics of the brown pumice type (dark color, lower vesicularity) could be used to interpret a more mafic composition, but this is not the case and suggests that variation in gas contents/degassing history is an important control on pumice textures (Rotella et al., 2014; Shea, 2017). Further study is required to confirm if the diversity of textures in the pumice raft reflects fluctuations in degassing rates resulting in a transition from an explosive to an effusive phase of eruption (e.g., Cordon Caulle 2012; Paisley et al., 2019).

We have shown no isotopic variation exists among Havre eruptive products (i.e., raft pumice, seafloor pumice, and lava flows), and they are isotopically similar to regional basalts in the Kermadec Arc Ridge (**Figure 7**). Therefore, the Havre 2012 rhyolite is interpreted here to be sourced from a relatively similar mantle as other eruptive products with similar isotopic ratios from the Kermadec Arc that have a range of compositions from basaltic andesite (e.g., Macauley island; Smith et al., 2003b) to rhyolite (e.g., Sandy Bay Tephra, Raoul and Healy; Smith et al., 2003a; Barker et al., 2013). This indicates no radiogenic crustal materials have been involved in rhyolite petrogenesis either through partial melting or assimilation-crystal fractionation (e.g., Timm et al., 2014).

Subsurface Sampling of the Havre Volcano

In this study, we take advantage of the 2012 eruption products to provide further insight into the magmatic system of the Havre volcano. A new observation reported here is that embedded lapilli-sized rock fragments are a common feature of the banded pumice, an abundant pumice type produced in the eruption and found in both the raft and on the seafloor deposits (Carey et al., 2018; Knafelc et al., 2020). Rock fragments are a characteristic feature of pyroclastic deposits produced by subaerial explosive eruptions reflecting excavation of wall rock from the conduit at the fragmentation depth (Suzuki-Kamata et al., 1993; Bryan et al., 2000). During an explosive eruption, the fragmentation depth can change (Dufek et al., 2012; Rotella et al., 2015). Therefore, the subsurface stratigraphy of the volcano can be sampled (Bryan et al., 2000; Suzuki-Kamata et al., 1993). A diversity of rock types is expected when explosive magma fragmentation occurs at depth in the conduit. If the embedded rock fragments represent a subsurface sampling of the conduit, then they provide snapshots of the older and deeper/buried parts of the Havre volcano and give insight into the longer-term magmatic system of the volcano. At present, sampling of Havre is restricted to the 2012 eruption and the few dredge samples collected in 2006 (Wright et al., 2006; see **Figure 1** in Knafelc et al., 2020).

Explosive eruptions and the rock fragment material they produce provide a useful tool to constrain the subsurface lithologies in the vent region of volcanoes. Distinct rock fragments and where independent geological constraints exist can be used to constrain vent location (Suzuki-Kamata et al., 1993; Wolff et al., 1999; Bryan et al., 2000; Torres-Hernández et al., 2006). The embedded rock fragments in the Havre banded pumice show significant lithological variety (e.g., basaltic to rhyolitic lavas) and variations in the degree of alteration (fresh to hydrothermally altered), providing for the first time sampling of the inner parts of the Havre volcano (**Figures 2**, **3**). The fresh, unaltered embedded rock fragments are interpreted to be shallow-derived, and the similarity of the Group 3 rock fragments to the 2012 rhyolite lava flows suggests similar rhyolite lavas may exist at the summit of Havre. Mafic blebs and inclusions observed in other Kermadec arc pumices (e.g., Raoul, Macauley, and Healy; Barker et al., 2013) record evidence of mafic recharge and/or magma mixing events. The rock fragments in the Havre pumice are angular, suggesting rock fragments are solidified before entrainment into the 2012 rhyolite. Therefore, the basaltic to dacitic rock fragment groups (Groups 1, 3, and 4) are interpreted to be older lavas that constructed the Havre edifice. Furthermore, the occurrence of both altered and unaltered rock fragments indicates the entrainment of rock material from different levels within the conduit. The embedded rock fragments are interpreted to reflect the explosive erosion of wall rock (Suzuki-Kamata et al., 1993; Bryan et al., 2000) at the fragmentation level in the conduit in response to magmatic volatile-driven magma fragmentation.

Comparison of Modelled Rhyolite-MELTS and Observed Mineral Assemblages and Compositions at Havre

Clinopyroxene

The same magnesian augite compositions determined by rhyolite-MELTS crystal fractionation models (**Figure 8A**) are similar to those in Group 1 embedded rock fragments and the Havre pumice augite antecryst population (Knafelc et al., 2020; **Figure 5G**).

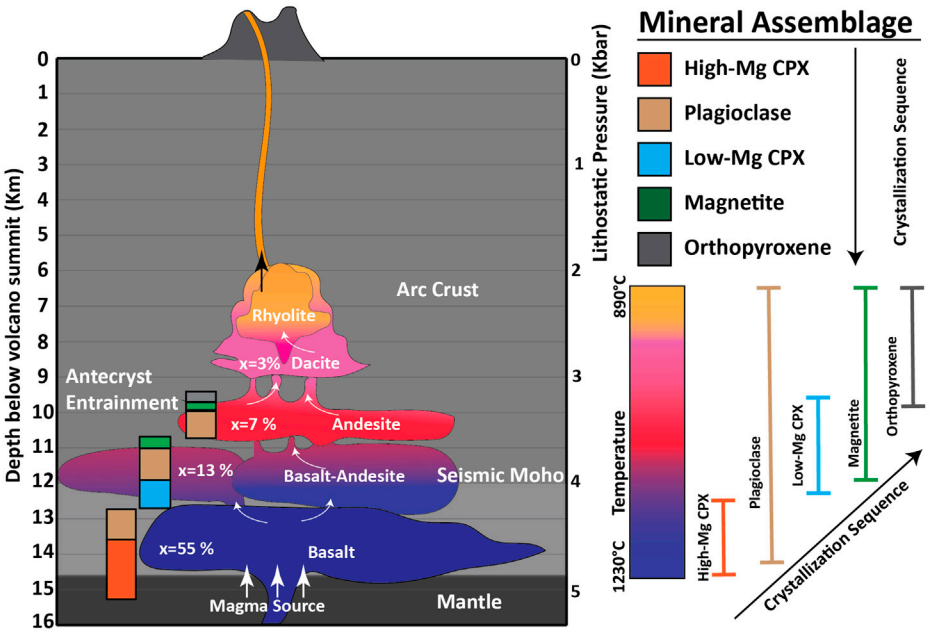

FIGURE 11 | Havre volcano magmatic plumbing system. This schematic section of the Havre magmatic plumbing system is scaled at depths and lithostatic pressure (determined by the density of average oceanic crust ~2.9 g cm^{-3}; Ridolfi et al., 2010). Crystallization and melt evolution from basalt to rhyolite progresses down pressure represented by stalling multiple magmatic lenses shown by multicolor gradients correlating to compositions and pressures from the rhyolite-MELTS model (basalt = blue; basaltic andesites = red to pink; andesite = green, dacite = pink to orange). Bar graphs depict the normalized proportion of minerals crystallized in each stepwise rhyolite-MELTS model from **Table 3**. The multicolor bar to the right represents the temperature of the melt in the magmatic system correlating with pressure from the calculated liquidus (~1,250°C, 5 kbar) to the pre-eruptive magmatic conditions for the 2012 eruption (~890°C, 2–3 kbar; Knafelc et al., 2020). To the right, the bracketed tie lines denote the range of temperatures at which each mineral phase crystallizes out in rhyolite-MELTS models (crystallization sequence goes from left to right). CPX is abbreviated for clinopyroxene.

Magnesian augite is calculated to crystallize from a melt that is basaltic to basaltic andesite in composition. The crystallization of magnesian augite occurs at temperatures of 1,230–1,190 to 1,100°C with initial crystallization temperatures varying dependent on pressures from 3 to 5 kbars (**Figure 9A**). Low-Mg augite antecryst compositions in the 2012 Havre pumice are produced in models that start with an initial basaltic andesite composition at NNO, 2.5 wt% H_2O from 1,100 to 1,020°C from 4 to 5 kbars. In lower pressure models (3.5–2 kb) of parental andesite composition, no clinopyroxene is crystallized. In higher pressure models, pigeonite is crystallized but is only rarely observed in the Havre 2012 rhyolite pumice (**Figure 6G**). The appearance of pigeonite in models could be due to some limitation of rhyolite-MELTS models at higher pressure or equilibration of pigeonite to orthopyroxene upon further cooling and increased oxygen fugacity (Grove and Juster, 1989). The latter explanation is preferred as Knafelc et al. (2020) observed a few pigeonite compositions occurring as resorbed cores in autocrystic orthopyroxene in the Havre 2012 rhyolite.

Orthopyroxene

In all models, orthopyroxene is the last phase to crystallize beginning at 1,000–1,010°C, and their calculated compositions overlap the natural compositional range of orthopyroxene from $En_{39}Fs_{23}Wo_{37}$ to $En_{54}Fs_{6}Wo_{40}$ found in the Havre pumice (Knafelc et al., 2020) and at crystallization temperatures of 950°–900°C (**Figure 9A**). At higher pressures in basaltic models, orthopyroxene only crystallizes at the 1,010–1,000°C temperature increment and is preferential to a pigeonite phase of similar Mg# (60–62). In our best fit models, orthopyroxene is only crystallized in models once the liquid has evolved to melt compositions >64 wt% SiO_2. Therefore, orthopyroxene is still a reliable autocrystic phase to constrain pre-eruptive temperatures of the Havre 2012 eruption as the models only crystallize the natural compositions close to pre-eruptive temperatures (890 ± 27°C) determined by opx-liquid geothermometry (Knafelc et al., 2020).

Plagioclase

Plagioclase crystallizes in all rhyolite-MELTS models from 1,230°C, and crystallization of this phase is suppressed in models outside the conditions presented here with increased pressures, reduced oxygen fugacities, and increased water concentrations. In the Havre raft pumice, plagioclase compositions range from An_{79} to An_{37}, with antecrystic cores showing disequilibrium textures for populations with An_{55}–An_{79} (Knafelc et al., 2020). The most mafic antecrystic plagioclase populations in the Havre raft pumice are first crystallized at 1,200°C in models from a parental basalt at high pressures (5 kbars), and the more abundant antecrystic plagioclase compositions are observed to be crystallizing from basaltic andesites (1,080–1,020°C) and andesitic rhyolite-MELTS models at temperatures above the 890 ± 27°C pre-eruptive temperatures (**Figure 9B**). In andesite models at 3.5 and 2 kbars, Havre 2012 autocrystic plagioclase compositions begin to crystallize at 950 and 930°C, respectively.

Liquid Compositions

Liquid lines of descent calculated for each model shown on an AFM diagram suggest a medium pressure tholeiitic crystallization trend is most likely to produce the Havre flank dacite composition (**Figure 9**; Yellow Star) after reaching 950°C (**Table 3**). Rhyolite-MELTS models closely replicate most major element oxides with increasing SiO_2 wt % concentrations following a crystallization trend to approximate the Havre flank dacite (**Figure 10**). Small discrepancies do appear with greater CaO wt% measured and lower alkali elements (Na_2O and K_2O) calculated in models compared to the actual composition of Havre dacite. The greatest differences in major element composition occur in intermediate composition models. This could be due to fewer constraints in phase equilibrium collaborations at these compositions and conditions in rhyolite-MELTS models (Gualda et al., 2012; Ghiorso and Gualda, 2015).

Implications for Havre Magmatic System

Fractionating Conditions

Here, we show the conditions and extent of fractional crystallization that could theoretically produce the Havre 2012 medium-K rhyolite from a low-K tholeiitic basalt. Rhyolite-MELTS modeling reveals key requirements for generating rhyolite: *1*) the basaltic parental melt must be genetically related to other Kermadec Arc ridge basalts; *2*) the basaltic parental magma follows a medium pressure tholeiitic crystallization trend that involves no early crystallization of olivine and a late appearance of magnetite; *3*) crystallization occurs at relatively low pressures (<5–2 kbar; *4*) the parental basalt initially contains a small about of volatiles (~1 wt% H_2O), consistent with an absence of hydrous mineralogy (i.e., amphiboles) in the 2012 rhyolite and embedded rock fragments; *5*) crystallization occurs in a step-wise/polybaric manner implying that progressively evolved melts must be stored at progressively shallower depths (9–15 km); and *6*) oxygen fugacities of the melt are required to increase from the parental basalt to erupted rhyolite (QFM- NNO +0.4).

Volume Considerations

The current paradigm for the generation of large batches of eruptive rhyolites through crystal fractionation involves magmatic systems dominated by crystal mush zones with silica-rich interstitial melts being extracted into a shallow magma body (Cashman et al., 2017). In order to generate larger volumes of crystal-poor silica-rich melts, it is thought that a parental basalt melt that undergoes 70%–80% crystallization must be 2.5–5 times greater in volume than the resulting evolved melt (Barker et al., 2013). Here, rhyolite-MELTS models suggest the extent of fractionation needed to crystallize in batches from basalt to basaltic andesite to andesite to dacite to rhyolite is roughly 55%, 29%, 22%, and 13%, respectively. In an end-member scenario where the total volume of parental basalt is stored in the magmatic plumbing system, we can then back-calculate a normalized crystallization proportion for each step of rhyolite-MELTS modeling. The normalized total extent of crystallization is then 78% from parental basalt to reach the Havre 2012 rhyolite composition, with crystallization proportions incrementally decreasing from basalt to basaltic andesite (~55%) to andesite (~13%) to dacite (7%) to rhyolite (3%). Therefore, to produce a 0.52 km^3 DRE volume of poor crystal rhyolite, up to approximately 2.6 km^3 of parental basalt magma (i.e., five times the volume of erupted rhyolite) is required to crystallize 78% to generate a rhyolite melt. This estimated volume of parental basalt could easily be stored in a vertical arrangement at several separate depths over the crustal thickness of 12–15 km beneath Havre volcano.

Havre Magmatic System

With these constraints in place at Havre, a potentially vertically extensive magmatic system (**Figure 11**) that spans 2–5 kb of pressure (6–15 km depth) may exist beneath Havre to generate a large volume of rhyolite by fractional crystallization. The magmatic plumbing system would be comprised of closely packed magmatic lenses or sills recording multiple stages of crystallization from which melt is extracted (Cashman et al., 2017; Marxer et al., 2022). Hourglass zoning of augite in the 2012 pumice (Knafelc et al., 2020) and some of the embedded rock fragments is a record of these crystals experiencing low degrees of undercooling due to either gradual recharge of parental basalt and/or slow magma ascent (Ubide et al., 2019) and then storage at varying depths in the magmatic plumbing system under Havre volcano. This model allows for more efficient density-driven melt extraction as each magmatic body is less likely to reach a packing threshold of ~50% or greater crystallinity, which is thought to prohibit interstitial melt extraction; such melt extraction over this crystallinity would require compaction, gas filter pressing, or external tectonic forces (Christopher et al., 2015).

Repeated episodes of polybaric crystallization and melt segregation can produce a volcanic edifice comprised of basaltic to rhyolitic composition lavas, as sampled here by the diversity of embedded rock fragments entrained into the banded raft pumice. A range of compositions is also observed in the pre-eruption dredge samples from basalt to rhyolite (Wright et al., 2006). The range in conditions (i.e., temperature, pressure, oxygen fugacity, and water contents) helps identify the deep-seated basaltic to andesite magma lenses as a source of antecrysts observed in the Havre pumice and older lavas, including magnesian augite and anorthite-rich plagioclase (**Figure 9**). Using the combined proportions of minerals crystallized in each step of rhyolite-MELTS models, the normalized proportions of minerals based on 78% crystallization from greatest to least is augite (55.7%), plagioclase (37.8%), magnetite (4.4%), and orthopyroxene (2.2%). Ultimately, petrogenetic major and trace element models and radiogenic isotope ratios, coupled with information from lithic clasts, provide a sampling of the longer-term magmatic system and suggest the erupted Havre 2012 rhyolite can be produced by extraction of a dacitic melt generated primarily by high-temperature crystallization of magnesian augite (En_{53-48}), anorthite rich plagioclase (An_{55-79}), and magnetite.

CONCLUSION

The Havre 2012 eruption evacuated a homogeneous body of medium-K rhyolite magma. There is little compositional variation detected between the raft pumice produced by the explosive eruption (Knafelc et al., 2022) and the seafloor pumice deposits (**Figure 4**). However, lavas produced by effusive eruptive phases thought to be

prior to pumice generation (Carey et al., 2018; Manga et al., 2018) have subtly lower silica contents (~71.5 wt% SiO_2) when compared to the rest of the eruption products (72.0–73.0 wt% SiO_2; **Figure 4D**). Despite five different raft pumice types, differences in appearance are textural (i.e., vesicle or microlite concentrations) rather than compositional and need further explanation that likely involves variable degassing and decompression trajectories during eruption (Mitchell et al., 2019; Knafelc et al., 2022). Embedded rock fragments are abundant in the banded raft pumice, rare in white pumice, and not observed in the other raft pumice types. A range of rock types are present, ranging from basaltic to rhyolitic lavas that range from being fresh to hydrothermally altered (**Figures 2**, **3** and **Supplementary Figure S1**). Based on this diversity, rock fragments are interpreted to be relatively shallow and derived by explosive erosion of the volcanic summit or conduit wall at varying fragmentation levels. These rock fragments provide the first indications of what comprises the interior of the Havre edifice and the range of magma compositions that erupted at Havre. Pb, Sr, and Nd isotopic homogeneity rules out the likelihood of rhyolite generation from partial melting of an external mantle (i.e., back-arc basin origins) or continental crust source (**Figure 7**). Rhyolite-MELTS models show that a fractional crystallization origin is possible by repeated episodes of polybaric crystallization and melt extraction to form magma stalled at progressively shallower levels in the Havre magmatic system (**Figure 11**). A parental dacite to the Havre rhyolite can be generated by high-temperature crystallization of magnesian augite clinopyroxene (En_{53-48}), anorthite-rich plagioclase (An_{55-79}), and magnetite over a range of pressures (2–5 kbar or 6–15 km) and oxygen fugacities (QFM-NNO). REE concentrations of regional basalts assumed to be a reasonable parental magma candidates to the Havre 2012 rhyolite are consistent with reverse-calculated REE patterns (**Figure 8**). Collectively, petrogenic major and trace element crystal fractionation models (rhyolite-MELTS) suggest extensive crystal fractionation (78%) of a ~2.6 km^3 body of dry low-K tholeiitic basalt sourced from the frontal Kermadec arc would be required to produce the 0.52 km^3 of erupted rhyolite during the Havre 2012 rhyolite submarine eruption.

DATA AVAILABILITY STATEMENT

The original contributions presented in the study are included in the article/**Supplementary Material**, further inquiries can be directed to the corresponding author.

AUTHOR CONTRIBUTIONS

This manuscript is a result of JK's Ph.D. research, with the majority of sample preparation, chemical analyses, data analysis, and production of figures completed by JK with the guidance/training of QUT's Central Analytical Research Facility (CARF) staff and Ph.D. supervisors DG, SB, and HC. DG and SB provided guidance on petrogenetic modeling and interpretations. HC performed analysis of mineral compositions by EPMA. MA performed isotopic chemical analysis and interpretation of these data. All authors contributed to refining/writing/editing of the manuscript.

FUNDING

JK was supported by a QUT PRA scholarship and an AINSE postgraduate research scholarship.

ACKNOWLEDGMENTS

We thank the Central Analytical Research Facility (CARF) at the Queensland University of Technology for EPMA, XRF, ICP-dissolution, and LA-ICP-MS chemical analysis. Access to CARF was supported by the Science and Engineering faculties at QUT. Balz Kamber and Sam Ghidan are thanked for performing ICP-MS dissolution for trace element data acquisition. Alan Bowe, Ken Betteridge, Jessica Martin, Brett Lewis, Adam Wright, and Eleanor Velasquez are thanked for their assistance with raft pumice collections. We thank George Kamenov for clean lab and MC-ICP-MS assistance. We also thank Samuel Platt and Katrina Bourke for their preliminary petrological investigation of the Havre embedded rock fragments that formed the basis of their QUT vacation research experience. We thank Simon J. Barker and Takashi Sano for their constructive feedback during the review process of this manuscript.

SUPPLEMENTARY MATERIAL

The Supplementary Material for this article can be found online at: https://www.frontiersin.org/articles/10.3389/feart.2022.886897/full#supplementary-material

REFERENCES

Anderson, M., Wanless, V. D., Perfit, M., Conrad, E., Gregg, P., Fornari, D., et al. (2021). Extreme Heterogeneity in Mid-Ocean Ridge Mantle Revealed in Lavas from the 8° 20′ N Near-Axis Seamount Chain. *Geochem. Geophys. Geosystems* 22 (1). doi:10.1029/2020gc009322

Annen, C., Blundy, J. D., and Sparks, R. S. J. (2006). The Genesis of Intermediate and Silicic Magmas in Deep Crustal Hot Zones. *J. Petrology* 47 (3), 505–539. doi:10.1093/petrology/egi084

Bachmann, O., and Bergantz, G. W. (2004). On the Origin of Crystal-Poor Rhyolites: Extracted from Batholithic Crystal Mushes. *J. Petrology* 45 (8), 1565–1582. doi:10.1093/petrology/egh019

Bachmann, O., and Bergantz, G. W. (2008). Rhyolites and Their Source Mushes Across Tectonic Settings. *J. Petrology* 49 (12), 2277–2285. doi:10.1093/petrology/egn068

Barker, S. J., Rotella, M. D., Wilson, C. J. N., Wright, I. C., and Wysoczanski, R. J. (2012). Contrasting Pyroclast Density Spectra from Subaerial and Submarine Silicic Eruptions in the Kermadec Arc: Implications for Eruption Processes and Dredge Sampling. *Bull. Volcanol.* 74 (6), 1425–1443. doi:10.1007/s00445-012-0604-2

Barker, S. J., Wilson, C. J. N., Baker, J. A., Millet, M.-A., Rotella, M. D., Wright, I. C., et al. (2013). Geochemistry and Petrogenesis of Silicic Magmas in the Intra-Oceanic Kermadec Arc. *J. Petrology* 54 (2), 351–391. doi:10.1093/petrology/egs071

Bassett, D., Kopp, H., Sutherland, R., Henrys, S., Watts, A. B., Timm, C., et al. (2016). Crustal Structure of the Kermadec Arc from MANGO Seismic Refraction Profiles. *J. Geophys. Res. Solid Earth* 121 (10), 7514–7546. doi:10.1002/2016jb013194

Brophy, J. G. (2008). A Study of Rare Earth Element (REE)-SiO2 Variations in Felsic Liquids Generated by Basalt Fractionation and Amphibolite Melting: A Potential Test for Discriminating Between the Two Different Processes. *Contrib. Mineral. Pet.* 156 (3), 337–357. doi:10.1007/s00410-008-0289-x

Bryan, S., Cas, R., and Martı, J. (2000). The 0.57 Ma Plinian Eruption of the Granadilla Member, Tenerife (Canary Islands): An Example of Complexity in Eruption Dynamics and Evolution. *J. Volcanol. Geotherm. Res.* 103 (1-4), 209–238. doi:10.1016/s0377-0273(00)00225-0

Bryan, S. E., Cook, A., Evans, J. P., Colls, P. W., Wells, M. G., Lawrence, M. G., et al. (2004). Pumice Rafting and Faunal Dispersion During 2001–2002 in the Southwest Pacific: Record of a Dacitic Submarine Explosive Eruption from Tonga. *Earth Planet. Sci. Lett.* 227 (1-2), 135–154. doi:10.1016/j.epsl.2004.08.009

Bryan, S. E., Cook, A. G., Evans, J. P., Hebden, K., Hurrey, L., Colls, P., et al. (2012). Rapid, Long-Distance Dispersal by Pumice Rafting. *PLoS One* 7 (7), e40583. doi:10.1371/journal.pone.0040583

Calder, E., Sparks, R., and Gardeweg, M. (2000). Erosion, Transport and Segregation of Pumice and Lithic Clasts in Pyroclastic Flows Inferred from Ignimbrite at Lascar Volcano, Chile. *J. Volcanol. Geotherm. Res.* 104 (1-4), 201–235. doi:10.1016/s0377-0273(00)00207-9

Carey, R., Soule, S. A., Manga, M., White, J., McPhie, J., Wysoczanski, R., et al. (2018). The Largest Deep-Ocean Silicic Volcanic Eruption of the Past Century. *Sci. Adv.* 4 (1), e1701121. doi:10.1126/sciadv.1701121

Carey, R. J., Wysoczanski, R., Wunderman, R., and Jutzeler, M. (2014). Discovery of the Largest Historic Silicic Submarine Eruption. *Eos, Trans. Am. Geophys. Union* 95 (19). doi:10.1002/2014eo190001

Cashman, K. V., Sparks, R. S., and Blundy, J. D. (2017). Vertically Extensive and Unstable Magmatic Systems: A Unified View of Igneous Processes. *Science* 355 (6331). doi:10.1126/science.aag3055

Christiansen, R. L., Calvert, A. T., and Grove, T. L. (2017). Geologic Field-Trip Guide to Mount Shasta Volcano, Northern California *(No. 2017-5022-K3)*. Reston, VA: US Geological Survey.

Christopher, T. E., Blundy, J., Cashman, K., Cole, P., Edmonds, M., Smith, P. J., et al. (2015). Crustal-Scale Degassing Due to Magma System Destabilization and Magma-Gas Decoupling at Soufrière Hills Volcano, Montserrat. *Geochem. Geophys. Geosyst.* 16 (9), 2797–2811. doi:10.1002/2015gc005791

Deering, C. D., Vogel, T. A., Patino, L. C., and Alvarado, G. E. (2007). Origin of Distinct Silicic Magma Types from the Guachipelín Caldera, NW Costa Rica: Evidence for Magma Mixing and Protracted Subvolcanic Residence. *J. Volcanol. Geotherm. Res.* 165 (3-4), 103–126. doi:10.1016/j.jvolgeores.2007.05.004

Dingwell, D. B., Lavallée, Y., Hess, K.-U., Flaws, A., Marti, J., Nichols, A. R. L., et al. (2016). Eruptive Shearing of Tube Pumice: Pure and Simple. *Solid Earth.* 7 (5), 1383–1393. doi:10.5194/se-7-1383-2016

Dufek, J., Manga, M., and Patel, A. (2012). Granular Disruption During Explosive Volcanic Eruptions. *Nat. Geosci.* 5 (8), 561–564. doi:10.1038/ngeo1524

Eggins, S. M., Woodhead, J. D., Kinsley, L. P. J., Mortimer, G. E., Sylvester, P., McCulloch, M. T., et al. (1997). A Simple Method for the Precise Determination of ≥ 40 Trace Elements in Geological Samples by ICPMS Using Enriched Isotope Internal Standardisation. *Chem. Geol.* 134 (4), 311–326. doi:10.1016/s0009-2541(96)00100-3

Ersoy, O., Aydar, E., Şen, E., and Gourgaud, A. (2019). Contrasting Fragmentation and Transportation Dynamics During the Emplacement of Dikkartın Rhyodacitic Dome; Erciyes Stratovolcano, Central Turkey. *Med. Geosc. Rev.* 1 (2), 223–242. doi:10.1007/s42990-019-00014-4

Geist, D., Howard, K. A., and Larson, P. (1995). The Generation of Oceanic Rhyolites by Crystal Fractionation: The Basalt-Rhyolite Association at Volc N Alcedo, Gal Pagos Archipelago. *J. Petrology* 36 (4), 965–982. doi:10.1093/petrology/36.4.965

Ghiorso, M. S., and Gualda, G. A. (2015). An H_2O–CO_2 Mixed Fluid Saturation Model Compatible with Rhyolite-MELTS. *Contributions Mineralogy Petrology* 169 (6), 1–30. doi:10.1007/s00410-015-1141-8

Gill, J. B. (1981). "What Is "Typical Calcalkaline Andesite" in *Orogenic Andesites and Plate Tectonics* (Berlin, Heidelberg: Springer), 1–12. doi:10.1007/978-3-642-68012-0_1

Gill, J., Hoernle, K., Todd, E., Hauff, F., Werner, R., Timm, C., et al. (2021). Basalt Geochemistry and Mantle Flow During Early Backarc Basin Evolution: Havre Trough and Kermadec Arc, Southwest Pacific. *Geochem. Geophys. Geosystems* 22 (2). doi:10.1029/2020gc009339

Goss, A., Perfit, M., Ridley, W., Rubin, K., Kamenov, G., Soule, S., et al. (2010). Geochemistry of Lavas from the 2005–2006 Eruption at the East Pacific Rise, 9 46′ N–9 56′ N: Implications for Ridge Crest Plumbing and Decadal Changes in Magma Chamber Compositions. *Geochem. Geophys. Geosystems* 11 (5). doi:10.1029/2009gc002977

Grove, T. L., and Juster, T. C. (1989). Experimental Investigations of Low-Ca Pyroxene Stability and Olivine-Pyroxene-Liquid Equilibria at 1-Atm in Natural Basaltic and Andesitic Liquids. *Contr. Mineral. Pet.* 103 (3), 287–305. doi:10.1007/bf00402916

Gualda, G. A. R., Ghiorso, M. S., Lemons, R. V., and Carley, T. L. (2012). Rhyolite-MELTS: A Modified Calibration of MELTS Optimized for Silica-Rich, Fluid-Bearing Magmatic Systems. *J. Petrology* 53 (5), 875–890. doi:10.1093/petrology/egr080

Haase, K., Krumm, S., Regelous, M., and Joachimski, M. (2011). Oxygen Isotope Evidence for the Formation of Silicic Kermadec Island Arc and Havre–Lau Backarc Magmas by Fractional Crystallisation. *Earth Planet. Sci. Lett.* 309 (3-4), 348–355. doi:10.1016/j.epsl.2011.07.014

Haase, K. M., Worthington, T. J., Stoffers, P., Garbe-Schönberg, D., and Wright, I. (2002). Mantle Dynamics, Element Recycling, and Magma Genesis Beneath the Kermadec Arc-Havre Trough. *Geochem.-Geophys.-Geosyst.* 3 (11), 1–22. doi:10.1029/2002gc000335

Hauff, F., Hoernle, K., Gill, J., Werner, R., Timm, C., Garbe-Schönberg, D., et al. (2021). R/V SONNE Cruise SO255 "VITIAZ": An Integrated Major Element, Trace Element and Sr-Nd-Pb-Hf Isotope Data Set of Volcanic Rocks from the Colville and Kermadec Ridges. Version 1.0. The Quaternary Kermadec Volcanic Front and the Havre Trough Backarc Basin.

Ikegami, F., McPhie, J., Carey, R., Mundana, R., Soule, A., and Jutzeler, M. (2018). The Eruption of Submarine Rhyolite Lavas and Domes in the Deep Ocean – Havre 2012, Kermadec Arc. *Front. Earth Sci.* 6. doi:10.3389/feart.2018.00147

Jutzeler, M., Marsh, R., Carey, R. J., White, J. D. L., Talling, P. J., and Karlstrom, L. (2014). On the Fate of Pumice Rafts Formed During the 2012 Havre Submarine Eruption. *Nat. Commun.* 5, 3660. doi:10.1038/ncomms4660

Kamber, B. S. (2009). Geochemical Fingerprinting: 40 Years of Analytical Development and Real World Applications. *Appl. Geochem.* 24 (6), 1074–1086. doi:10.1016/j.apgeochem.2009.02.012

Kamber, B. S., and Gladu, A. H. (2009). Comparison of Pb Purification by Anion-Exchange Resin Methods and Assessment of Long-Term Reproducibility of Th/U/Pb Ratio Measurements by Quadrupole ICP-MS. *Geostand. Geoanalytical Res.* 33 (2), 169–181. doi:10.1111/j.1751-908x.2009.00911.x

Knafelc, J., Bryan, S. E., Gust, D., and Cathey, H. E. (2020). Defining Pre-Eruptive Conditions of the Havre 2012 Submarine Rhyolite Eruption Using Crystal Archives. *Front. Earth Sci.* 8. doi:10.3389/feart.2020.00310

Knafelc, J., Bryan, S. E., Jones, M. W. M., Gust, D., Mallmann, G., Cathey, H. E., et al. (2022). Havre 2012 Pink Pumice Is Evidence of a Short-Lived, Deep-Sea, Magnetite Nanolite-Driven Explosive Eruption. *Commun. Earth Environ.* 3 (1), 19. doi:10.1038/s43247-022-00355-3

Kuno, H. (1959). Origin of Cenozoic Petrographic Provinces of Japan and Surrounding Areas. *Bull. Volcanol.* 20 (1), 37–76. doi:10.1007/bf02596571

Le Maitre, R. W. (1989). A Classification of Igneous Rocks and Glossary of Terms. Recommendations of the International Union of Geological Sciences Subcommission on the Systematics of Igneous Rocks, 193.

Lindsley, D. H., and Andersen, D. J. (1983). A Two-Pyroxene Thermometer. *J. Geophys. Res.* 88 (S02), A887–A906. doi:10.1029/jb088is02p0a887

Manga, M., Fauria, K. E., Lin, C., Mitchell, S. J., Jones, M., Conway, C. E., et al. (2018). The Pumice Raft-Forming 2012 Havre Submarine Eruption Was Effusive. *Earth Planet. Sci. Lett.* 489, 49–58. doi:10.1016/j.epsl.2018.02.025

Marxer, F., Ulmer, P., and Müntener, O. (2022). Polybaric Fractional Crystallisation of Arc Magmas: An Experimental Study Simulating Trans-Crustal Magmatic Systems. *Contributions Mineralogy Petrology* 177 (1), 1–36. doi:10.1007/s00410-021-01856-8

McCulloch, M. T., Kyser, T. K., Woodhead, J. D., and Kinsley, L. (1994). Pb?Sr?Nd? O Isotopic Constraints on the Origin of Rhyolites from the Taupo Volcanic Zone of New Zealand: Evidence for Assimilation Followed by Fractionation from Basalt. *Contr. Mineral. Pet.* 115 (3), 303–312. doi:10.1007/bf00310769

McDonough, W. F., McCulloch, M. T., and Sun, S. S. (1985). Isotopic and Geochemical Systematics in Tertiary-Recent Basalts from Southeastern Australia and Implications for the Evolution of the Sub-Continental Lithosphere. *Geochimica Cosmochimica Acta* 49 (10), 2051–2067. doi:10.1016/0016-7037(85)90063-8

McLennan, S. M. (1989). "Archean Sedimentary Rocks and the Archean Mantle," in *Workshop on the Archean Mantle*, 57.

Mitchell, S. J., Fauria, K. E., Houghton, B. F., and Carey, R. J. (2021). Sink or Float: Microtextural Controls on the Fate of Pumice Deposition During the 2012 Submarine Havre Eruption. *Bull. Volcanol.* 83 (11), 1–20. doi:10.1007/s00445-021-01497-6

Mitchell, S. J., Houghton, B. F., Carey, R. J., Manga, M., Fauria, K. E., Jones, M. R., et al. (2019). Submarine Giant Pumice: A Window into the Shallow Conduit Dynamics of a Recent Silicic Eruption. *Bull. Volcanol.* 81 (7). doi:10.1007/s00445-019-1298-5

Miyashiro, A. (1974). Volcanic Rock Series in Island Arcs and Active Continental Margins. *Am. J. Sci.* 274 (4), 321–355. doi:10.2475/ajs.274.4.321

Moriizumi, M., Nakashima, S., Okumura, S., and Yamanoi, Y. (2008). Color-Change Processes of a Plinian Pumice and Experimental Constraints of Color-Change Kinetics in Air of an Obsidian. *Bull. Volcanol.* 71 (1), 1–13. doi:10.1007/s00445-008-0202-5

Murch, A. P., White, J. D. L., and Carey, R. J. (2019). Characteristics and Deposit Stratigraphy of Submarine-Erupted Silicic Ash, Havre Volcano, Kermadec Arc, New Zealand. *Front. Earth Sci.* 7. doi:10.3389/feart.2019.00001

Murch, A. P., White, J. D. L., and Carey, R. J. (2019). Unusual Fluidal Behavior of a Silicic Magma During Fragmentation in a Deep Subaqueous Eruption, Havre Volcano, Southwestern Pacific Ocean. *Geology* 47 (5), 487–490. doi:10.1130/g45657.1

Paisley, R., Berlo, K., Whattam, J., Schipper, C. I., and Tuffen, H. (2019). Degassing-Induced Chemical Heterogeneity at the 2011-2012 Cordón Caulle Eruption. *Volcanica* 2 (2), 211–237. doi:10.30909/vol.02.02.211237

Paton, C., Hellstrom, J., Paul, B., Woodhead, J., and Hergt, J. (2011). Iolite: Freeware for the Visualisation and Processing of Mass Spectrometric Data. *J. Anal. At. Spectrom.* 26 (12), 2508–2518. doi:10.1039/c1ja10172b

Plank, T., and Langmuir, C. H. (1998). The Chemical Composition of Subducting Sediment and its Consequences for the Crust and Mantle. *Chem. Geol.* 145 (3-4), 325–394. doi:10.1016/s0009-2541(97)00150-2

Reagan, M., Turner, S., Handley, H., Turner, M., Beier, C., Caulfield, J., et al. (2017). ^{210}Pb-^{226}Ra Disequilibria in Young Gas-Laden Magmas. *Sci. Rep.* 7 (1), 1–12. doi:10.1038/srep45186

Ridolfi, F., Renzulli, A., and Puerini, M. (2010). Stability and Chemical Equilibrium of Amphibole in Calc-Alkaline Magmas: An Overview, New Thermobarometric Formulations and Application to Subduction-Related Volcanoes. *Contrib. Mineral. Pet.* 160 (1), 45–66. doi:10.1007/s00410-009-0465-7

Rotella, M. D., Wilson, C. J., Barker, S. J., Cashman, K. V., Houghton, B. F., and Wright, I. C. (2014). Bubble Development in Explosive Silicic Eruptions: Insights from Pyroclast Vesicularity Textures from Raoul Volcano (Kermadec Arc). *Bull. Volcanol.* 76 (8), 1–24. doi:10.1007/s00445-014-0826-6

Rotella, M. D., Wilson, C. J. N., Barker, S. J., Ian Schipper, C., Wright, I. C., and Wysoczanski, R. J. (2015). Dynamics of Deep Submarine Silicic Explosive Eruptions in the Kermadec Arc, as Reflected in Pumice Vesicularity Textures. *J. Volcanol. Geotherm. Res.* 301, 314–332. doi:10.1016/j.jvolgeores.2015.05.021

Shea, T. (2017). Bubble Nucleation in Magmas: A Dominantly Heterogeneous Process? *J. Volcanol. Geotherm. Res.* 343, 155–170. doi:10.1016/j.jvolgeores.2017.06.025

Shea, T., Gurioli, L., and Houghton, B. F. (2012). Transitions between Fall Phases and Pyroclastic Density Currents during the AD 79 Eruption at Vesuvius: Building a Transient Conduit Model from the Textural and Volatile Record. *Bull. Volcanol.* 74 (10), 2363–2381. doi:10.1007/s00445-012-0668-z

Shea, T., Hellebrand, E., Gurioli, L., and Tuffen, H. (2014). Conduit- to Localized-Scale Degassing during Plinian Eruptions: Insights from Major Element and Volatile (Cl and H2O) Analyses within Vesuvius AD 79 Pumice. *J. Petrology* 55 (2), 315–344. doi:10.1093/petrology/egt069

Smith, I. E. M., Worthington, T. J., Stewart, R. B., Price, R. C., and Gamble, J. A. (2003). Felsic Volcanism in the Kermadec Arc, SW Pacific: Crustal Recycling in an Oceanic Setting. *Geol. Soc. Lond. Spec. Publ.* 219 (1), 99–118. doi:10.1144/gsl.sp.2003.219.01.05

Smith, I. E., and Price, R. C. (2006). The Tonga–Kermadec Arc and Havre–Lau Back-Arc System: Their Role in the Development of Tectonic and Magmatic Models for the Western Pacific. *J. Volcanol. Geotherm. Res.* 156 (3-4), 315–331. doi:10.1016/j.jvolgeores.2006.03.006

Smith, I. E., Stewart, R. B., and Price, R. C. (2003). The Petrology of a Large Intra-Oceanic Silicic Eruption: The Sandy Bay Tephra, Kermadec Arc, Southwest Pacific. *J. Volcanol. Geotherm. Res.* 124 (3-4), 173–194. doi:10.1016/s0377-0273(03)00040-4

Sun, C., and Liang, Y. (2012). Distribution of REE Between Clinopyroxene and Basaltic Melt Along a Mantle Adiabat: Effects of Major Element Composition, Water, and Temperature. *Contrib. Mineral. Pet.* 163 (5), 807–823. doi:10.1007/s00410-011-0700-x

Sun, S.-S., and McDonough, W. F. (1989). Chemical and Isotopic Systematics of Oceanic Basalts: Implications for Mantle Composition and Processes. *Geol. Soc. Lond. Spec. Publ.* 42 (1), 313–345. doi:10.1144/gsl.sp.1989.042.01.19

Suzuki-Kamata, K., Kamata, H., and Bacon, C. R. (1993). Evolution of the Caldera-Forming Eruption at Crater Lake, Oregon, Indicated by Component Analysis of Embedded Rock Fragments. *J. Geophys. Res. Solid Earth* 98 (B8), 14059–14074.

Tait, S., Thomas, R., Gardner, J., and Jaupart, C. (1998). Constraints on Cooling Rates and Permeabilities of Pumice in an Explosive Eruption Jet from Colour and Magnetic Mineralogy. *J. Volcanol. Geotherm. Res.* 86 (1-4), 79–91. doi:10.1016/s0377-0273(98)00075-4

Timm, C., Davy, B., Haase, K., Hoernle, K. A., Graham, I. J., De Ronde, C. E., et al. (2014). Subduction of the Oceanic Hikurangi Plateau and its Impact on the Kermadec Arc. *Nat. Commun.* 5 (1), 4923–4929. doi:10.1038/ncomms5923

Timm, C., de Ronde, C. E. J., Leybourne, M. I., Layton-Matthews, D., and Graham, I. J. (2012). Sources of Chalcophile and Siderophile Elements in Kermadec Arc Lavas. *Econ. Geol.* 107 (8), 1527–1538. doi:10.2113/econgeo.107.8.1527

Torres-Hernández, J. R., Labarthe-Hernández, G., Aguillón-Robles, A., Gómez-Anguiano, M., and Mata-Segura, J. L. (2006). The Pyroclastic Dikes of the Tertiary San Luis Potosí Volcanic Field: Implications on the Emplacement of Panalillo Ignimbrite. *GeofInt* 45 (4), 243–253. doi:10.22201/igeof.00167169p.2006.45.4.161

Tozer, B., Sandwell, D. T., Smith, W. H. F., Olson, C., Beale, J. R., and Wessel, P. (2019). Global Bathymetry and Topography at 15 Arc Sec: SRTM15+. *Earth Space Sci.* 6 (10), 1847–1864. doi:10.1029/2019ea000658

Ubide, T., Mollo, S., Zhao, J.-x., Nazzari, M., and Scarlato, P. (2019). Sector-Zoned Clinopyroxene as a Recorder of Magma History, Eruption Triggers, and Ascent Rates. *Geochimica Cosmochimica Acta* 251, 265–283. doi:10.1016/j.gca.2019.02.021

Ulrich, T., Kamber, B. S., Woodhead, J. D., and Spencer, L. A. (2010). Long-Term Observations of Isotope Ratio Accuracy and Reproducibility Using Quadrupole ICP-MS. *Geostand. Geoanalytical Res.* 34 (2), 161–174. doi:10.1111/j.1751-908x.2010.00046.x

White, W. M., Hofmann, A. W., and Puchelt, H. (1987). Isotope Geochemistry of Pacific Mid-Ocean Ridge Basalt. *J. Geophys. Res.* 92 (B6), 4881. doi:10.1029/jb092ib06p04881

Wolff, J. A., Ramos, F. C., and Davidson, J. P. (1999). Sr Isotope Disequilibrium During Differentiation of the Bandelier Tuff: Constraints on the Crystallization of a Large Rhyolitic Magma Chamber. *Geol.* 27 (6), 495–498. doi:10.1130/0091-7613(1999)027<0495:sidddo>2.3.co;2

Woodhead, J. D., Hellstrom, J., Hergt, J. M., Greig, A., and Maas, R. (2007). Isotopic and Elemental Imaging of Geological Materials by Laser Ablation Inductively Coupled Plasma-Mass Spectrometry. *Geostand. Geoanalytical Res.* 31 (4), 331–343.

Wright, I., Worthington, T., and Gamble, J. (2006). New Multibeam Mapping and Geochemistry of the 30–35 S Sector, and Overview, of Southern Kermadec Arc Volcanism. *J. Volcanol. Geotherm. Res.* 149 (3-4), 263–296. doi:10.1016/j.jvolgeores.2005.03.021

Conflict of Interest: The authors declare that the research was conducted in the absence of any commercial or financial relationships that could be construed as a potential conflict of interest.

Publisher's Note: All claims expressed in this article are solely those of the authors and do not necessarily represent those of their affiliated organizations or those of the publisher, the editors, and the reviewers. Any product that may be evaluated in this article, or claim that may be made by its manufacturer, is not guaranteed or endorsed by the publisher.